Title: Brassinosteroid coordinates cell layer interactions in plants via cell wall and tissue mechanics

Authors: Robert Kelly-Bellow†[1], Karen Lee†[1], Richard Kennaway[1], J. Elaine Barclay[1], Annabel Whibley[1], Claire Bushell[1], Jamie Spooner[1], Man Yu[1], Paul Brett[2], Baldeep Kular[2], Shujing Cheng[3], Jinfang Chu[3,4], Ting Xu[5], Brendan Lane[6], James Fitzsimons[7], Yongbiao Xue[5], Richard Smith*[6], Christopher D. Whitewoods[1,7]*, Enrico Coen[1]*

Affiliations:

[1]Department of Cell and Developmental Biology, John Innes Centre, Norwich Research Park; Colney Lane, Norwich, NR4 7UH, UK.

[2]Department of Biochemistry and Metabolism, John Innes Centre, Norwich Research Park; Colney Lane, Norwich, NR4 7UH, UK.

[3]National Centre for Plant Gene Research (Beijing), Institute of Genetics and Developmental Biology, Chinese Academy of Sciences; Beijing 100101, China.

[4]College of Advanced Agricultural Sciences, University of Chinese Academy of Sciences; Beijing 100039, China.

[5]State Key Laboratory of Plant Cell and Chromosome Engineering, Institute of Genetics and Developmental Biology, Chinese Academy of Sciences; Beijing 100101, China.

[6]Department of Computational and Systems Biology, John Innes Centre, Norwich Research Park; Colney Lane, Norwich, NR4 7UH, UK.

[7]Sainsbury Laboratory, University of Cambridge; Cambridge CB2 1LR, UK.

†These authors contributed equally to this work.

*Corresponding authors

Abstract

Growth coordination between cell layers is essential for development of most multicellular organisms. Coordination may be mediated by molecular signalling and/or mechanical connectivity between cells, but how genes modify mechanical interactions between layers is unknown. Here we show that genes driving brassinosteroid synthesis promote growth of internal tissue by reducing mechanical epidermal constraint. We identify a brassinosteroid-deficient dwarf mutant in the aquatic plant *Utricularia gibba* with twisted internal tissue, likely caused by a mechanical constraint from a slow-growing epidermis. We test this hypothesis by showing that a brassinosteroid mutant in *Arabidopsis* enhances epidermal crack formation, indicative of increased tissue stress. We propose that by remodeling cell walls, brassinosteroids reduce epidermal constraint, showing how genes can control growth coordination between layers via mechanics.

One-Sentence Summary

Internal twists in a mutant carnivorous plant reveal how genes control growth coordination via tissue mechanics.

Main Text

Many multicellular organisms are formed from multiple cell layers, raising the question of how growth is coordinated between layers to produce an integrated final form. In plants, evidence from genetic chimeras and from layer-specific modification of gene function, show that genes active in one layer can act non-autonomously to influence growth in other layers (*1-4*). Non-autonomy could be explained through chemical signalling between layers and/or mechanical interactions.

Mechanics may act non-autonomously through the generation of tissue stresses (*5*), demonstrated experimentally by Hofmeister more than 150 years ago (*6*). To understand the origin of tissue stresses, consider a cylindrical tissue in which cells are tightly stuck together, with all cells having the same size, turgor, wall material properties and wall thickness (Fig. 1A). If cell walls are anisotropic, such that they yield more readily in the vertical orientation, the vertical component of turgor forces within to each cell can cause stresses (highlighted for three cells with black double-headed arrows) that produce axial growth. There are no growth conflicts between cells. However, if the epidermal walls (purple, Fig. 1B) yield less to turgor (e.g. because they are thicker or less extensible than inner walls), an epidermal growth constraint is generated, and load is transferred from inner to outer walls. Each cell experiences mechanical stresses caused by the cell's own turgor (cell-autonomous stresses), and by mechanical effects from surrounding tissue (non-cell-autonomous stresses), termed tissue stresses. Whereas the cell-autonomous stress is always tensile, by our definition tissue stresses can be tensile or compressive: the epidermis is under tissue tension (divergent red arrows, Fig. 1B), whereas internal regions are under tissue compression (convergent blue arrows).

Tissue stresses can be revealed by immediate outward re-curvature of median slices through internodes, or by the formation of epidermal cracks when adhesion between cells is weakened (*6-8*). They can be quantified by stretching detached epidermal tissue to the point that it restores its original length (*9, 10*). However, little is known about how tissue stresses are controlled genetically and thus the role they may play in non-cell-autonomous gene action. Here we address this problem through the analysis of dwarf mutants in the aquatic plant *Utricularia gibba* and the terrestrial plant *Arabidopsis thaliana*.

U. gibba **dwarf has twisted internal tissue**

U. gibba is a carnivorous plant with a spiral vegetative growing tip, comprising an apex that produces stolons bearing filiform leaves and traps (*11*) (Fig. 2A). The stolons and leaves have internal air spaces that allow the plant to float just below the water surface. To obtain developmental mutants in *U. gibba*, we carried out ethyl methanesulfonate mutagenesis. Obtaining large numbers of progeny proved difficult because of poor seed set and germination rates. Rather than mutagenizing seed, we therefore mutagenized small stolon explants and grew each on to flowering (see Methods for details). M1 seed was collected from 441 explants and gave M2 phenotypes including altered traps, absent traps, reduced leaf and stolon growth, long flower spurs, spiky leaves, multiple traps on leaves, and fasciation. One M2 family contained two dwarf plants, and self-seed from a wild-type sib gave 37 wild type, 9 dwarf, and 3 extreme-dwarf plants (Fig. 2, A to C), consistent with segregation of two recessive mutations: *dwarf* and *enhancer of dwarf*.

Both the dwarf and extreme-dwarf plants had short internodes, short leaves and small traps (Fig. 2, A to D). To follow their development, we numbered internodes sequentially relative to the spiral apex, with internode 1 corresponding to the first clearly visible internode to emerge from the apex (fig. S1). Wild-type internode length increased until about internode 4, after which it plateaued to give a mature internode length of about 2mm (Fig. 2E). By contrast dwarf and extreme dwarf plants exhibited very little growth after internode 1, generating mature internode lengths of about 0.7mm and 0.3mm (Fig. 2E). Epidermal cells of mutant stolons were shorter and smaller than those of wild type (Fig. 2, F to J). Measurements of cell lengths parallel to the stolon axis indicated that 70% of the reduction in dwarf internode length was caused by reduced longitudinal growth after cell division arrest (fig. S2A). Further reduction in internode length in extreme dwarf was caused by reduced growth prior to division arrest. In addition to reduced internode length, both dwarf and extreme dwarf exhibited a significant increase in stolon circumference and number of epidermal cells in transverse sections compared to wild type, indicating increased radial and circumferential growth prior to division arrest (fig. S2B and C).

We next determined the phenotype of internal tissues. Wild-type stolons had a cylindrical epidermis (purple, Fig. 3C) connected by 5-6 straight “blades” (cyan) to an axial cylinder of large cells (yellow) surrounding a vascular bundle (orange), with air spaces (magenta) between the blades (Fig. 3, A to C). Dwarf stolons had smaller air spaces, twisted blades and a sinuous contorted vascular bundle (Fig. 3, D to F). Extreme-dwarf stolons had smaller air spaces and less twisted vasculature than dwarf (Fig. 3, G to I). Both dwarf and extreme dwarf plants sank in water, presumably because of their reduced air spaces.

The twisted internal tissue of the dwarf plants might be caused by a contorted pattern of early vascular and blade cell-type specification, or by altered tissue growth after specification had occurred. To distinguish these possibilities, we determined the developmental timing of the twisted phenotype in dwarf plants. Straight vasculature cell types surrounded by blade and air spaces were evident at internodes 0 in dwarf (Fig. 3J), as in wild type (fig. S3A). Twisted vascular tissue in dwarf plants was only observed from internode 4 onwards (Fig. 3K). Contortions of the blade were evident in dwarf mutants earlier, at internode 1, as tissue strips running perpendicular to the vascular axis in longitudinal sections (blue arrow, Fig. 3J). These blade contortions were only seen after air spaces had formed. Thus, contortion and twisting of internal tissue in dwarf plants arose through altered growth after cell-type specification and air space formation, leading to excess vascular length compared to epidermal length (fig. S2D). In extreme dwarf plants, which showed little contortion, organized vasculature and surrounding tissue was evident in early internodes, but air spaces were not (fig. S3B).

Twisted dwarf phenotype explained by epidermal constraint

To evaluate hypotheses that might account for both the internal twisting and shortened internode length of *dwarf* mutants, we modelled tissue growth using continuum mechanics. For these purposes we distinguish between two types of regional growth: specified and resultant (*12*). Specified growth corresponds to the growth driven by a cell's own turgor, in mechanical isolation from other cells. Resultant growth corresponds to the growth generated when tissue stresses, which act non-cell-autonomously, are also factored in. Computational models allow tissue stresses and resultant growth to be calculated from an input pattern of specified growth rates and orientations.

We modelled a small length of *U. gibba* stolon as a stiff cylindrical epidermal sheet connected by blades to an axial core (Fig. 4, A to C and fig. S10, A and B). Specified growth was oriented parallel to an axial (initially vertical) polarity field (arrows, Fig. 4A). To reduce boundary effects, each stolon end was constrained to remain flat and horizontal.

If all regions had the same specified growth rate, the cylinder elongated without generation of tissue stresses or twisting of internal tissue (Fig. 4, D to F). If specified growth rate was set to zero in the epidermis, the epidermal constraint caused a dwarf phenotype (Fig. 4, G and H). Tissue tension was generated in the epidermis (red, Fig. 4I), and tissue compression in the blades and core (blue, Fig. 4, I and J). The tissue tension caused the epidermis to grow to some extent, despite its specified growth rate being zero (compare epidermal resultant growth rate, Fig. 4K, with specified growth rate Fig. 4G). Conversely, tissue compression in blades and core caused lower resultant growth rate than that specified (compare Fig. 4L with Fig. 4H). The tissue stresses also caused twisting of blades and core (Fig. 4, M to P, Movie 1). Thus, reduced specified growth rate in the epidermis captured both the dwarf phenotype and internal contortion.

Twisting of the axial core still occurred when blades were removed from a middle segment of the cylinder (fig. S4, A to F), showing that tissue compression could be transmitted to the core from above and below. No twisting occurred if the cylinder was solid (fig. S4, G to K), showing that air spaces were needed to accommodate buckling, and accounting for the reduced twisting observed in extreme dwarf plants. Restricting specified growth to the axial core led to a dwarf phenotype and sinuous core but little twisting of the blades (fig. S4, L and M). Restricting specified growth to the blades gave a dwarf phenotype with twisted blades, but little twisting of the core (fig. S4, N to P). Radial specified growth of the blades led to blade twisting, but cylinder elongation and axial core straightness were not affected (fig. S4, Q to V). Thus, both the dwarfism and internal axial and blade twisting could be most readily accounted for by reduced specified growth rate of the epidermis alone.

***DWARF* encodes a brassinosteroid biosynthetic enzyme**

To understand the molecular basis of the *dwarf* mutant, we sequenced the wild-type progenitor, 33 wild-type, 10 dwarf and 3 extreme-dwarf segregants. Only one SNP was absent from the progenitor, heterozygous or absent in wild type segregants, and homozygous in all mutants, indicating that it was located in the *DWARF* gene. Extreme-dwarf plants carried 4 additional SNPs absent from the progenitor (Table S1) that were candidate mutations in *ENHANCER OF DWARF*. Plants homozygous for *enhancer of dwarf* and heterozygous or homozygous for *DWARF* were scored as wild type, suggesting that the *enhancer of dwarf* mutation alone did not have a strong phenotypic effect. However, the mutation may have caused a subtle phenotype that we missed when initially scoring the families.

The *DWARF* SNP introduced an early stop codon in a gene encoding a cytochrome P450 90B1 enzyme, which catalyses the C22-alpha-hydroxylation step in the brassinosteroid biosynthesis pathway (*13*). This gene is homologous to *DWARF4* (*DWF4*) in *Arabidopsis*, which affects cell area and cell anisotropy in a similar way to *U. gibba DWARF* (*14*, *15*). Brassinosteroid precursors after the C22-alpha-hydroxylation step were undetectable or at a low level in *dwarf* mutants, whereas a precursor before the step was present (fig. S5). Inhibiting brassinosteroid biosynthesis in wild type using brassinazole led to short stolons, smaller cells and contorted vasculature, similar to *dwarf* mutants (fig. S6). Adding brassinosteroid, by growing mutants in epibrassinolide, rescued dwarf and partially rescued extreme dwarf plants (fig. S6). Thus, *DWARF* likely encodes a brassinosteroid biosynthesis gene.

To determine the timing of brassinosteroid action, we tracked dwarf stolons after treatment with epibrassinolide (Fig. 4S). Internodes that were not readily visible when the treatment began, because they were concealed within the spiral vegetative shoot tip or had not yet initiated, were assigned consecutive negative numbers, starting from 0. These internodes grew to a length similar to those of mature wild type (Fig. 4T). Internodes 1 to 5 also showed a significant length increase in response to treatment ($p < 0.05$), with the magnitude of the increase declining with internode number. Thus, brassinosteroid likely acts from around internode 0, when cell division is nearing arrest, until around internode 5, by which stage cell elongation has arrested in wild-type. However, we cannot rule out the possibility that internodes above 5 are impermeable to exogenous brassinosteroid.

Arabidopsis brassinosteroid mutant has elevated tissue stresses

Our experimental and modelling results indicate that brassinosteroid promotes *U. gibba* stolon growth from just before cell division arrest by counteracting an epidermal constraint, thus reducing tissue stresses. If generally applicable, this hypothesis predicts that *Arabidopsis dwf4* mutants should also exhibit elevated tissue stresses. However, the effect of these stresses might be masked because *Arabidopsis* stems are solid and therefore lack of air spaces to accommodate buckling (fig. S4, G to K). To determine whether tissue stresses are enhanced in *dwf4* mutants, we therefore exploited the *quasimodo2-1* (*qua2-1*) mutation, which weakens cell-cell adhesion (*16*). As illustrated in Fig. 1B (red arrows), tissue stresses generated a force that acts to pull epidermal cells apart. In wild-type *Arabidopsis*, cell-cell adhesion is strong enough to resist this force, but in *qua2* mutants epidermal cracks are observed between cells in dark-grown hypocotyls, confirming that epidermal tissue tension is present (*17*, *18*). If brassinosteroid normally acts to reduce tissue tension, cracks are predicted to be exacerbated in *qua2 dwf4* double mutants, or in *qua2* mutants treated with a brassinosteroid inhibitor.

To test these predictions, we intercrossed *dwf4* and *qua2-1* mutant lines. About 1/16 (58/885) of the F2 dark-grown seedlings exhibited a striking novel phenotype: hypocotyls were dwarf and seemed devoid of epidermis (Fig. 5, A and B), unlike *qua2-1* single mutants which showed small epidermal cracks at a similar stage (Fig. 5C). To clarify the developmental origin of the double mutant phenotype, we imaged seedlings at different days following germination. Seedlings of *dwf4 qua2* were indistinguishable from *dwf4* seedlings until about 3 days after stratification, when wide cracks appeared in the double mutant (Fig. 5D). These cracks were much larger than those observed in *qua2* single mutants at the same stage (Fig. 5E). By 5 days, the cracks in *dwf4 qua2* had enlarged to the extent that much of the epidermis was no longer evident (Fig. 5B). Crack formation was also enhanced when *qua2* single mutants were grown in the presence of a brassinosteroid inhibitor**,** brassinazole (fig. S7). These results thus support the hypothesis that brassinosteroid promotes stem growth by counteracting an epidermal constraint.

To further validate this interpretation, we modelled the growth of a solid cylinder with a stiff epidermis in which cracks can form when tension exceeds a threshold value. Uniform specified growth rate gave elongation without tissue stresses or cracks (Fig. 5, F and G); whereas low epidermal specified growth led to reduced elongation, elevated tissue stresses and crack formation (Fig. 5H and I).

Release from epidermal constraint by wall remodeling

The above results raise the question of how brassinosteroid reduces epidermal constraint. The most obvious source of an epidermal constraint is the thick outer wall of the epidermal cells (*6*). A constraining outer wall is also consistent with the concave shape of the outer wall in epidermal cells released by crack formation (purple arrows, Fig.5, C to E). Outer epidermal walls of *U. gibba dwarf* stolons were about 2-3 times thicker than inner walls at internode 1 (fig. S8, D and F), by which time growth had ceased (Fig. 2E). Outer epidermal walls of *A. thaliana dwf4* dark-grown hypocotyls were about 20 times thicker than inner walls at 4 days after stratification (fig.

S8, C and E), by which time growth had largely ceased (fig. S9). Similar wall thicknesses were observed for wild types at comparable stages (fig. S8, A, B, E and F), even though growth continued afterwards, suggesting that brassinosteroid does not reduce epidermal constraint primarily by altering wall thickness.

A possible mechanism for reduction of epidermal constraint is wall loosening: brassinosteroids promote hypocotyl elongation within 6 h of application through increased wall relaxation properties (i.e. wall loosening) (*19*, *20*), possibly via phosphorylation of plasma membrane H^+-ATPase (*21*). To explore the possible contribution of wall loosening, we modelled hypocotyl tissue growth at the cellular level. A segment of hypocotyl was modelled as a vertical cylinder of tightly attached cells of similar size and under the same turgor, (Fig. 5J). Wall growth via creep (*22*) was simulated by converting a proportion of reversible elastic wall strain, above a yield threshold, into irreversible strain at each time step. The proportion corresponded to the extensibility of the wall. Walls were seven times stiffer (seven times greater Young's modulus) in the transverse compared to longitudinal orientation, leading to vertical specified growth.

If all cell walls had the same material properties, the cylinder elongated with uniform specified growth rates (Fig. 5K), low tissue stresses (Fig. 5L), and uniform longitudinal wall stresses (Fig. 5M). Introducing an epidermal fracture caused rounding of the cell ends but did not cause further cell separation (Fig. 5N, position of fracture arrowed). Setting the outer epidermal wall to be 10 times thicker than inner walls, lowered epidermal specified growth rate (Fig. 5O). The growth constraint generated longitudinal epidermal tissue tension and internal tissue compression (Fig. 5P). Resultant longitudinal wall stresses were uniform, but lower than previously (compare Fig. 5Q with Fig. 5M). The cylinder therefore grew less, capturing the *dwf4* phenotype. Introducing a wide epidermal fracture (8 cells wide) released epidermal cell ends to peel back (Fig. 5R, Movie 2), capturing the *dwf4 qua2* phenotype (Fig. 5D).

To simulate wild type, the thick outer wall was loosened by increasing its extensibility and reducing its yield threshold. This modification increased epidermal specified growth rate (compare Fig. 5S with 5O), lowered tissue stresses (compare Fig. 5T with 5P) and raised longitudinal wall stresses of internal tissue (compare Fig. 5U with 5Q). The cylinder therefore elongated more than the *dwf4* simulation, capturing the wild-type phenotype. Introducing a narrow epidermal fracture (2 cells wide) led to released epidermal cell ends peeling back (Fig. 5V), capturing the *qua2* phenotype (Fig. 5C). Thus, brassinosteroid likely acts, at least in part, by loosening of the thick outer wall, counteracting the epidermal constraint.

In addition to wall thickness, epidermal constraint may be further enhanced by the orientation of microfibrils, which are less transverse in outer compared to inner walls for wild-type *Arabidopsis* hypocotyls (*23*). Brassinosteroid treatment can cause microtubules of the outer epidermal plasma membrane to orient more transversely (*24*, *25*). Thus, brassinosteroid may reduce epidermal constraint by remodeling the thick outer wall in two ways: wall loosening and reducing the proportion of longitudinally-oriented microfibrils. Such an effect on microfibril orientation might explain why *Utricularia dwarf* mutants have wider stolons (fig. S2, B and C). The differential properties of the outer epidermal wall (e.g. thickness, extensibility, microfibril orientation) may depend on cell polarity factors that confer differences between outer and inner cell faces (*26*-*28*).

Conclusion

When brassinosteroid synthesis or perception genes are expressed only in the epidermal cell layer of *Arabidopsis* brassinosteroid mutants, a near wild-type phenotype is generated, even though these genes are normally expressed in both epidermis and ground tissue (*4, 29*). Our results indicate that this non-autonomous effect of epidermal brassinosteroid gene expression on resultant growth of internal tissue is mediated, at least in part, by release of internal tissue from epidermal mechanical constraint. Mechanical interactions between cell layers also play a role in animal development, such as formation of crocodile skin cracks (*30*) and intestinal villi (*31*). Here we show how genes may modify tissue layer interactions by changing cellular growth properties and thus tissue stresses. Gene activity may therefore have coordinated effects on tissue development not only via molecular signaling, but also via mechanics.

Online material includes Materials and Methods
Supplementary text
Figs. S1 to S10
Tables S1 and S2
References (*32-49*)
Movies 1 and 2

FIGURES

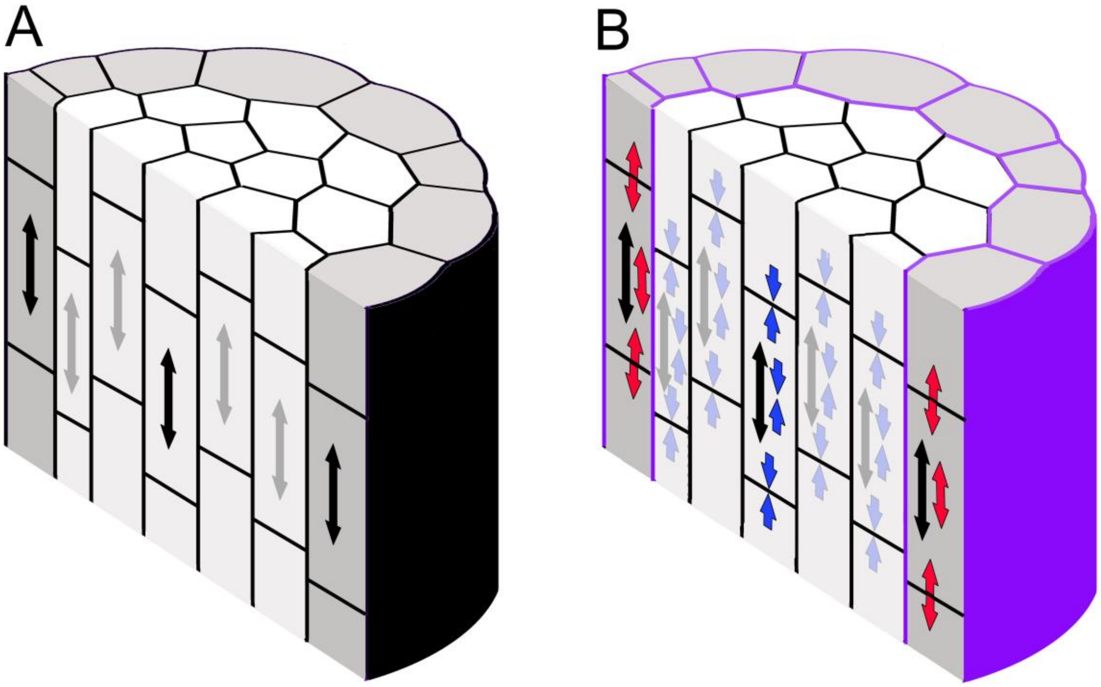

Fig. 1. Origin of tissue stresses

Section through a stem with epidermal cells in grey and cell walls black. (**A**). All cell walls have the same material properties. Vertical component of turgor forces autonomous to each cell cause stresses (highlighted for three cells with black double-headed arrows) that produce axial growth. There are no growth conflicts between cells and tissue stresses are zero. (**B**) If the epidermal walls (purple) yield less to turgor, an epidermal growth constraint is generated. Each cell now experiences two types of stress: cell autonomous stress caused by the cell's own turgor (black double-headed arrows), and tissue stress caused by mechanical effects from surrounding tissue. Tissue stresses can be tensile (divergent red arrows) or compressive (convergent blue arrows).

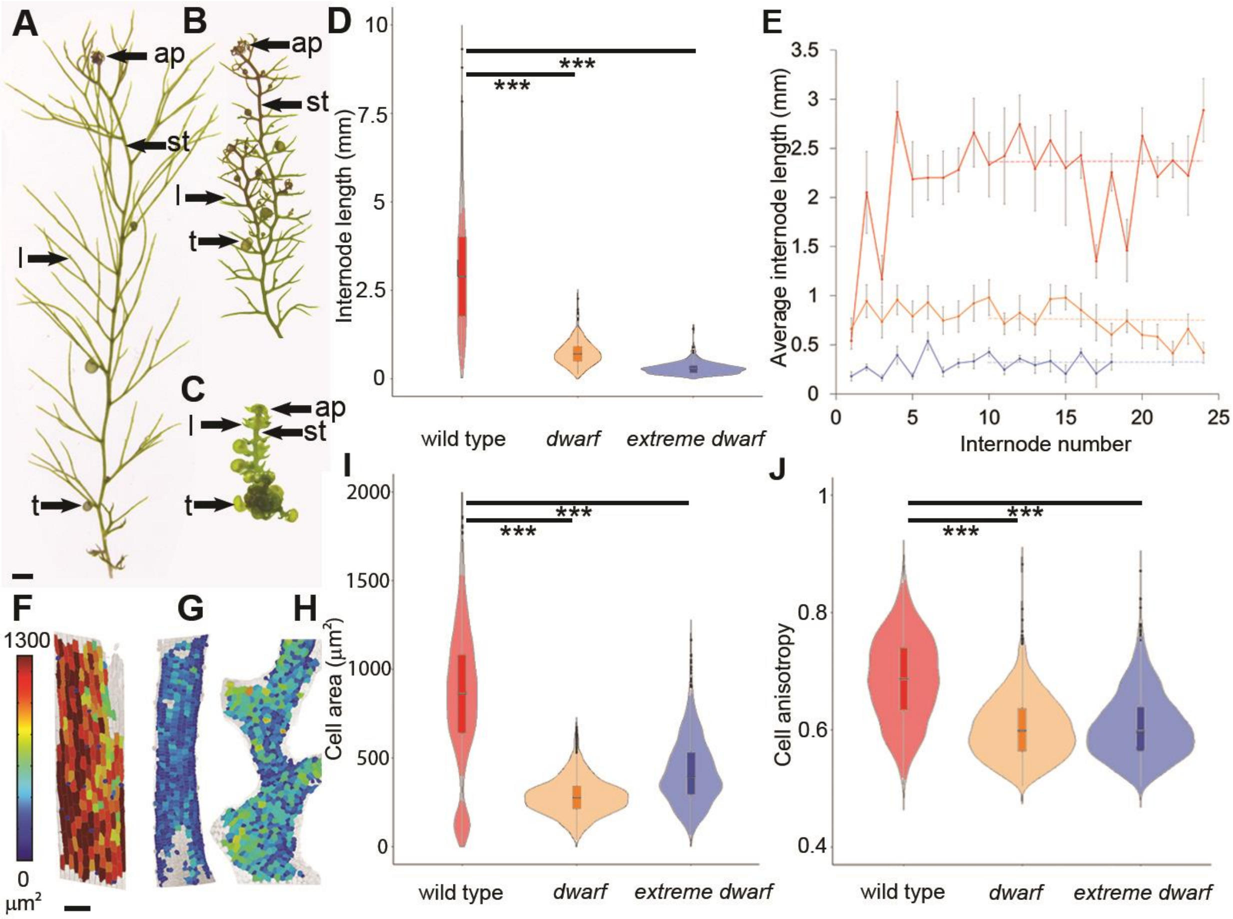

Fig. 2. External phenotype of U. gibba wild type and dwarf mutants.

(**A** to **C**) *U. gibba* vegetative plants comprise a spiral apex (ap), filiform leaves (l), stolons (st) and traps (t). (A) Wild type. (B) Dwarf. (C) Extreme dwarf. Scale bar 1 mm. (**D**) Violin plots of wild-type ($\bar{x}$ = 3.07 mm +/- 0.11 (SEM), n=10), dwarf ($\bar{x}$ = 0.72 mm +/- 0.02 (SEM), n=10) and extreme dwarf ($\bar{x}$ = 0.29 mm +/- 0.01 (SEM), n=13) mature internode lengths from plants grown in continuous culture. Block indicates interquartile range and horizontal line the mean. Both mutants have reduced lengths compared to wild type ($p < 0.001$, ***). (**E**) Internode lengths from growing explants of wild type (red), dwarf (orange) and extreme dwarf (blue) plotted against internode number. Dashed line shows mean from internode 10 onwards (n > 4). (**F** to **H**) Heat maps of cell area in mature stolons of wild type (F), dwarf (G) and extreme dwarf (H) mutants. Scale bar 100 µm. (**I** and **J**) Violin plots of cell area (I) and cell anisotropy (cell maximum length/(cell maximum length + cell minimum length)) (J) of mature stolons of wild type (n=1817 cells from 8 plants), dwarf (n=2289 cells from 5 plants) and extreme dwarf (n=1494 cells from 4 plants). Both mutants have significantly lower values than wild type.

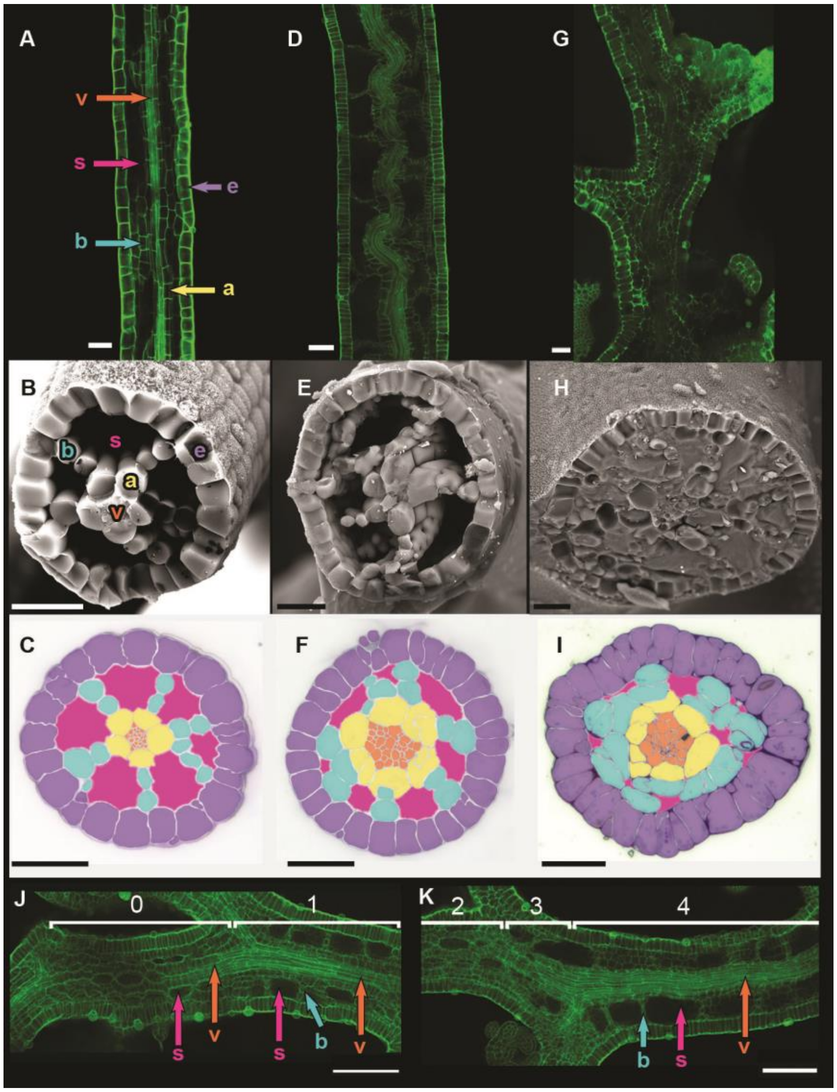

Fig. 3. Internal phenotype of *U. gibba* wild type and dwarf mutants.

Wild type (**A** to **C**), dwarf (**D** to **F**) and extreme dwarf (**G** to **I**) longitudinal confocal sections (A, D and G), freeze-fracture scanning electron microscopy (B, E and H) and toluidine-blue-stained transverse sections (C, F, and I). Arrows or cells color-coded purple for epidermis (e), cyan for blades (b), magenta for air spaces (s), yellow for axial core (a), and orange for vasculature (v). Scale bars 50 µm. (**J** and **K**) Confocal Z-slice of early dwarf internodes. Scale bar 100 µm.

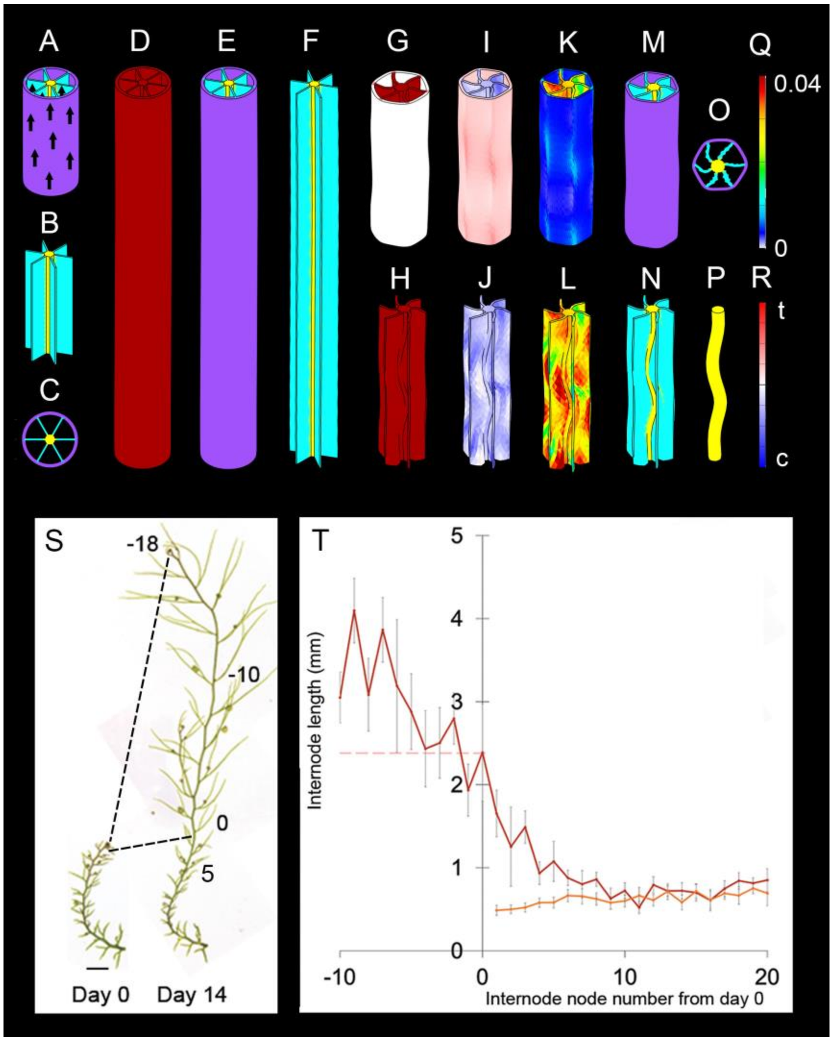

Fig. 4. Simulations of *U. gibba* wild type and dwarf mutant and timing of brassinosteroid action.

(**A**) Initial state for wild-type and dwarf mutant models - epidermis (purple), blades (cyan) and axial core (yellow). Arrows indicate polarity. (**B**) Initial state without epidermis. (**C**) Transverse slice of (A). (**D**) Final state of wild type simulation, color-coded for specified growth rate, which is uniformly high. (**E**) As (D), color-coded for tissue type. (**G**) Final state for simulation of dwarf mutant, color-coded for specified growth rate, which is excluded from the epidermis and gives reduced elongation. (**I**) As (G), color-coded for tissue stresses. (**K**) As (G), color-coded for resultant growth rate. (**M**) As (G), color-coded for tissue type. (**H, J, L, N)** as (G, I, K, M) with epidermis clipped away. (**O**) Transverse slice of (M). (**P**) as (M) showing axial core only. (**Q**) Color scale for specified and resultant growth rates, in strain per time step of simulation. (**R**) Color scale for tissue stresses, with red indicating tension (t) and blue compression (c). (**S**) A dwarf explant imaged on day 0 and day 14 after treatment with 0.01 µM epibrassinolide. Internode numbers labelled on day 14. Scale bar 5 mm. (**T**) Average internode lengths of dwarf explants (day 0, solid orange line), and 14 days (day 14, solid brown line), (n ≥ 10). Day 14 internode 0 to -10 lengths were not significantly different from the mean of Fig. 2E (red dashed line). Error bars show standard error of the mean.

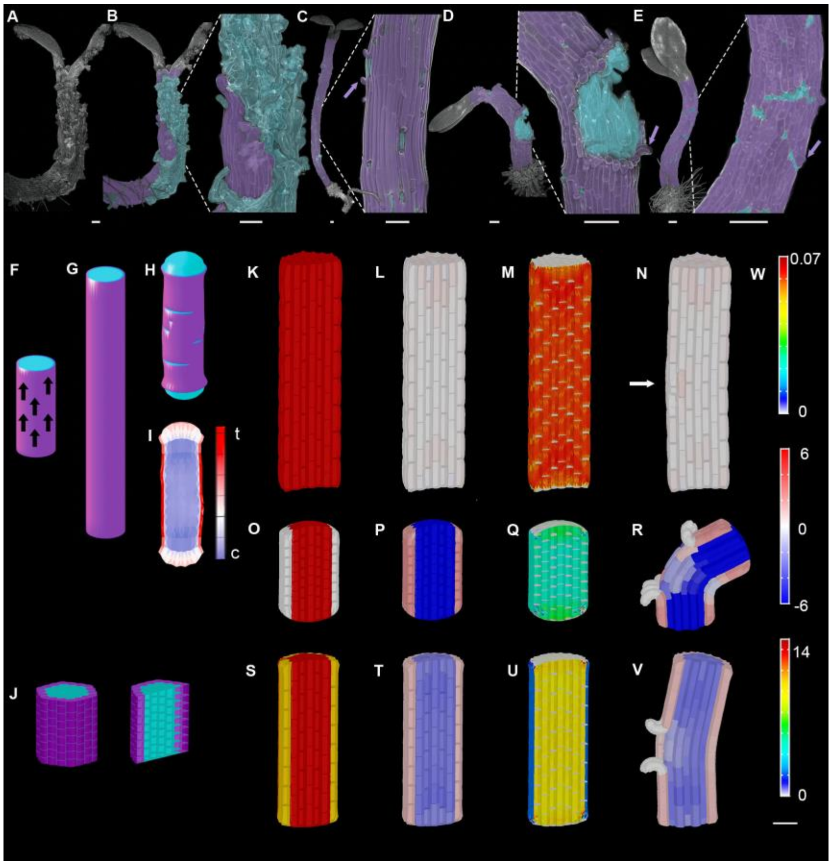

Fig. 5. Epidermal cracks in *Arabidopsis qua2-1 dwf4* compared to *qua2-1* and explanatory computational models.

(A-C) Confocal images 5 days after stratification. (A) *qua2-1 dwf4* double mutant (B) *qua2-1* dwf4 shown in (A) with cells artificially colored for clarity: purple = epidermal cells and cyan = interior cells. It is possible that the cyan-colored cells include some disorganised epidermal cells. Close-up shown on right. (C) *qua2-1* single mutant with a close up of a region with cracks. **(D, E)** Confocal images 3 days after stratification. (D) *qua2-1 dwf4* double mutant (E) *qua2-1* single mutant. Scale bars 100 µm. Purple arrows highlight curled free ends of epidermal cells. (**F** to **I**) Tissue-level computer simulations. (F) Initial state, with epidermis purple and inner regions in cyan. Arrows indicate polarity. (G) Final state with all regions having the same specified growth parallel to polarity, leading to elongation without epidermal cracking. (H) Final state with reduced specified growth in epidermis, leads to a shorter cylinder and epidermal cracks. (I) Longitudinal section through (H), showing longitudinal tissue tension (t) in red and compression (c) in blue. (**J** to **W)** Cellular-level computer simulations. (J) Initial state, with outer epidermal wall dark purple, epidermis purple and inner tissue cyan. (K-V) Final state. (K-N) All cell walls same thickness and material properties. (O-R) Outer epidermal wall ten times thicker. (S-V) Outer wall ten times thicker, with higher extensibility and reduced yield threshold. (N,R,V) Epidermal fracture introduced at an early stage. Fracture is 2 cells wide for (N and R) and 8 cells wide for (V). (K, O, S) Specified growth rate. (L, P, T, N, R, V) Tissue stresses. (M, Q, U) Resultant longitudinal wall stresses. (W) Color scales. Top: Specified growth rate (7 % per time step?). Middle: Tissue stresses (MPa). Bottom: Longitudinal wall stresses (MPa). Scale bar 50µm.

Movie 1: Tissue-level growth simulation of *Utricularia dwarf* mutant.

Initial stolon showing arrangement of axial core (yellow), blades (cyan) and epidermis (purple). Specified growth is high (red) except in the epidermis, where it is zero (white). After growth, the axial core and blades have become contorted.

Movie 2: Cellular-level growth simulation of *Arabidopsis qua2 dwf4* and *qua2*

Tissue stresses are displayed for a section and then whole stem segment. Epidermal growth constraint causes tissue tension (red) in the epidermis and tissue compression (blue) in the interior. The *qua2 dwf4* mutant has greater tissue stresses because, in the absence of brassinosteroid, the thick outer wall is no longer loosened. After introduction of an epidermal fracture (8 cells wide for *qua2 dwf4*, and 2 cells wide for *qua2*), the released epidermal cell ends peel back because of the slower-growing thick outer cell wall, exposing the interior, and the stem bends.

References

1. S. Hake, B. R. Char, Cell-cell interactions during plant development. *Genes & Development* **11**, 1087-1097 (1997).
2. M. H. Frank, D. H. Chitwood, Plant chimeras: The good, the bad, and the ‘Bizzaria’. *Developmental Biology* **419**, 41-53 (2016).
3. R. A. Tilney-Bassett, *Plant Chimeras*. (Edward Arnold (Publishers) Ltd., 1986).
4. S. Savaldi-Goldstein, C. Peto, J. Chory, The epidermis both drives and restricts plant shoot growth. *Nature* **446**, 199 (2007).
5. Z. Hejnowicz, A. Sievers, Tissue stresses in organs of herbaceous plants I. Poisson ratios of tissues and their role in determination of the stresses. *J Exp Bot* **289**, 1035-1043 (1995).
6. U. Kutschera, K. J. Niklas, The epidermal-growth-control theory of stem elongation: an old and a new perspective. *J Plant Physiol* **164**, 1395-1409 (2007).
7. W. S. Peters, A. D. Tomos, The history of tissue tension. *Ann Bot* **77**, 657-665 (1996).
8. S. Verger, Y. Long, A. Boudaoud, O. Hamant, A tension-adhesion feedback loop in plant epidermis. *eLife* **7**, (2018).
9. Z. Hejnowicz, A. Sievers, Tissue stresses in organs of herbaceous plants II. Determination in three dimensions in the hypocotyl of sunflower. *J Exp Bot* **46**, 1045-1053 (1995).
10. U. Kutschera, Determination of the longitudinal tissue stresses in the growing and non-growing regions of sunflower hypocotyls. *J. Plant Physiol.* **138**, 460-465 (1991).
11. P. Taylor, *The Genus Utricularia : a taxonomic monograph*. (Royal Botanic Gardens, London, 1989).

12. E. Coen, R. Kennaway, C. Whitewoods, On genes and form. *Development* **144**, 4203-4213 (2017).
13. S. Fujioka *et al.*, Identification of a New Brassinosteroid, Cathasterone, in Cultured Cells of Catharanthus roseus as a Biosynthetic Precursor of Teasterone. *Bioscience, Biotechnology, and Biochemistry* **59**, 1543-1547 (1995).
14. R. Azpiroz, Y. Wu, J. C. LoCascio, K. A. Feldmann, An Arabidopsis Brassinosteroid-Dependent Mutant Is Blocked in Cell Elongation. *Plant Cell* **10**, 219-230 (1998).
15. S. Choe *et al.*, The DWF4 gene of Arabidopsis encodes a cytochrome P450 that mediates multiple 22alpha-hydroxylation steps in brassinosteroid biosynthesis. *Plant Cell* **10**, 231-243 (1998).
16. S. Verger, S. Chabout, E. Gineau, G. Mouille, Cell adhesion in plants is under the control of putative O-fucosyltransferases. *Development* **143**, 2536-2540 (2016).
17. G. Mouille *et al.*, Homogalacturonan synthesis in Arabidopsis thaliana requires a Golgi-localized protein with a putative methyltransferase domain. *The Plant Journal* **50**, 605-614 (2007).
18. S. Verger, Y. Long, A. Boudaoud, O. Hamant, A tension-adhesion feedback loop in plant epidermis. *Elife* **7**, e34460 (2018).
19. D. M. Zurek, T. C. Rayle Dl Fau - McMorris, S. D. McMorris Tc Fau - Clouse, S. D. Clouse, Investigation of Gene Expression, Growth Kinetics, and Wall Extensibility during Brassinosteroid-Regulated Stem Elongation. *Plant physiology* **104**, 505–513 (1994).
20. T. W. Wang, D. J. Cosgrove, R. N. Arteca, Brassinosteroid Stimulation of Hypocotyl Elongation and Wall Relaxation in Pakchoi (Brassica chinensis cv Lei-Choi). *Plant Physiol* **101**, 965-968 (1993).
21. A. Minami, K. Takahashi, S. I. Inoue, Y. Tada, T. Kinoshita, Brassinosteroid Induces Phosphorylation of the Plasma Membrane H+-ATPase during Hypocotyl Elongation in Arabidopsis thaliana. *Plant Cell Physiol* **60**, 935-944 (2019).
22. E. Coen, D. J. Cosgrove, The mechanics of plant morphogenesis. *Science* **379**, eade8055 (2023).
23. E. F. Crowell *et al.*, Differential regulation of cellulose orientation at the inner and outer face of epidermal cells in the Arabidopsis hypocotyl. *Plant Cell* **23**, 2592-2605 (2011).
24. X. Wang *et al.*, Arabidopsis microtubule destabilizing protein40 is involved in brassinosteroid regulation of hypocotyl elongation. *Plant Cell* **24**, 4012-4025 (2012).
25. M. Catterou *et al.*, Brassinosteroids, microtubules and cell elongation in Arabidopsis thaliana. II. Effects of brassinosteroids on microtubules and cell elongation in the bul1 mutant. *Planta* **212**, 673-683 (2001).
26. J. Takano *et al.*, Polar localization and degradation of Arabidopsis boron transporters through distinct trafficking pathways. *Proc Natl Acad Sci U S A* **107**, 5220-5225 (2010).
27. Ł. Łangowski, K. Růžička, S. Naramoto, J. Kleine-Vehn, J. Friml, Trafficking to the Outer Polar Domain Defines the Root-Soil Interface. *Current Biology* **20**, 904-908 (2010).
28. V. Gorelova, J. Sprakel, D. Weijers, Plant cell polarity as the nexus of tissue mechanics and morphogenesis. *Nat Plants* **7**, 1548-1559 (2021).
29. D. M. Friedrichsen, C. A. Joazeiro, J. Li, T. Hunter, J. Chory, Brassinosteroid-insensitive-1 is a ubiquitously expressed leucine-rich repeat receptor serine/threonine kinase. *Plant Physiol* **123**, 1247-1256 (2000).

30. M. C. Milinkovitch *et al.*, Crocodile Head Scales Are Not Developmental Units But Emerge from Physical Cracking. *Science* **339**, 78-81 (2013).
31. A. E. Shyer *et al.*, Villification: how the gut gets its villi. *Science* **342**, 212-218 (2013).
32. T. Asami *et al.*, Characterization of brassinazole, a triazole-type brassinosteroid biosynthesis inhibitor. *Plant Physiology* **123**, 93-100 (2000).
33. E. Truernit *et al.*, High-resolution whole-mount imaging of three-dimensional tissue organization and gene expression enables the study of Phloem development and structure in Arabidopsis. *Plant Cell* **20**, 1494-1503 (2008).
34. S. Strauss *et al.*, Using positional information to provide context for biological image analysis with MorphoGraphX 2.0. *Elife* **11**, e72601 (2022).
35. R. Wightman, S. Wallis, P. Aston, Hydathode pit development in the alpine plant Saxifraga cochlearis. *Flora* **233**, 99-108 (2017).
36. H. Li, N. A. Trzaskalski, R. J. N. Emery, Analysis of Brassinosteroids in Soybean Seeds and Leaves by Liquid Chromatography-Tandem Mass Spectrometry. *The Open Plant Science Journal* **10**, 100-109 (2017).
37. F. Huo *et al.*, A new derivatization approach for the rapid and sensitive analysis of brassinosteroids by using ultra high performance liquid chromatography-electrospray ionization triple quadrupole mass spectrometry. *Talanta* **99**, 420-425 (2012).
38. P. Xin, J. Yan, J. Fan, J. Chu, C. Yan, An improved simplified high-sensitivity quantification method for determining brassinosteroids in different tissues of rice and Arabidopsis. *Plant Physiology* **162**, 2056-2066 (2013).
39. P. Xin *et al.*, A Tailored High-Efficiency Sample Pretreatment Method for Simultaneous Quantification of 10 Classes of Known Endogenous Phytohormones. *Plant Communications* **1**, 100047 (2020).
40. J. P. Blumenstiel *et al.*, Identification of EMS-Induced Mutations in *Drosophila melanogaster* by Whole-Genome Sequencing. *Genetics* **182**, 25-32 (2009).
41. T. Lan *et al.*, Long-read sequencing uncovers the adaptive topography of a carnivorous plant genome. *Proceedings of the National Academy of Sciences* **114**, E4435-E4441 (2017).
42. D. J. Cosgrove, Diffuse Growth of Plant Cell Walls. *Plant Physiology* **176**, 16-27 (2018).
43. J. A. Lockhart, An analysis of irreversible plant cell elongation. *J Theor Biol* **8**, 264-275 (1965).
44. M. Majda, N. Trozzi, G. Mosca, R. S. Smith, How Cell Geometry and Cellular Patterning Influence Tissue Stiffness. *International Journal of Molecular Sciences* **23**, 5651 (2022).
45. H. Hofhuis *et al.*, Morphomechanical Innovation Drives Explosive Seed Dispersal. *Cell* **166**, 222-233 (2016).
46. G. W. Bassel *et al.*, Mechanical constraints imposed by 3D cellular geometry and arrangement modulate growth patterns in the Arabidopsis embryo. *Proceedings of the National Academy of Sciences* **111**, 8685-8690 (2014).
47. E. Hernandez-Lagana *et al.*, Organ geometry channels reproductive cell fate in the Arabidopsis ovule primordium. *Elife* **10**, e66031 (2021).
48. A. Bajguz, M. Chmur, D. Gruszka, Comprehensive Overview of the Brassinosteroid Biosynthesis Pathways: Substrates, Products, Inhibitors, and Connections. *Frontiers in Plant Science* **11**, (2020).

49. E. Ibarra-Laclette *et al.*, Architecture and evolution of a minute plant genome. *Nature* **498**, 94 (2013).

Acknowledgments: We would like to thank B. and P. Steward at The Fly Trap Plants and T. Bailey from the Carnivorous Plant Society for plants, seeds, and advice and Mateusz Majda for *qua2-1* seeds, Eva Wegel and Sergio Lopez JIC Bioimaging for help with light microscopy, Ray Wightman for help with freeze-fracture SEM, Lionel Perkins and JIC Horticulture team for large scale *U. gibba* cultivation, Gabriella Mosca for MorphoMechanX and Desmond Bradley for critical reading of the manuscript. **Funding:** This work was supported by European Research Council grant (323028-CarnoMorph) and Biotechnology and Biological Sciences Research Council grants (BBS/E/J/000PR9787, BB/M023117/1, BB/L008920/1) awarded to EC. **Author contributions:** RK-B, KL, JEB, MY, PB, BK, SC, JC, TX, BL, JF, YX, RS and CDW contributed biological experiments, data analysis and conceptualization, RK, RS and EC computational modelling, RK and RS software development, KL, CB, JS, MY and CDW development of *U. gibba* resources, RK-B and AW bioinformatic analysis, and EC supervision, funding acquisition and conceptualization. **Data and materials availability:** All data is available in the main text or the supplementary materials. Code is available at the following website: https://github.com/JIC-Enrico-Coen/Cell_Layer_Interactions_2023. **Competing interests:** Authors declare that they have no competing interests.

Supplementary Materials for

Brassinosteroid coordinates cell layer interactions in plants via cell wall and tissue mechanics

Robert Kelly-Bellow†[1], Karen Lee†[1], Richard Kennaway[1], J. Elaine Barclay[1], Annabel Whibley[1], Claire Bushell[1], Jamie Spooner[1], Man Yu[1], Paul Brett[2], Baldeep Kular[2], Shujing Cheng[3], Jinfang Chu[3,4], Ting Xu[5], Brendan Lane[6], James Fitzsimmons[7], Yongbiao Xue[5], Richard Smith[6*], Christopher D. Whitewoods[1,7]*, Enrico Coen[1]*

†These authors contributed equally to this work.
Correspondence to: richard.smith@jic.ac.uk, chris.whitewoods@slcu.ac.uk, enrico.coen@jic.ac.uk

This PDF file includes:

Materials and Methods
Supplementary Text
Figs. S1 to S10
Tables S1 and S2
References (*32-49*)
Movies 1 and 2

Materials and Methods

U. gibba plant material and growth conditions

Tissue culture

Utricularia gibba seeds of wild-type plants were purchased from Fly Trap Plants (Bergh Apton, UK). Plant material was grown in liquid ½ MS plant tissue culture media (0.22 % Murashige and Skoog Medium (MS) (Duchefa Biochemie M0233), 2.5 % sucrose, pH 5.8) and maintained in controlled environment room (CER) conditions at 23 ±1 °C, light at an intensity of 180 µmol/m^2/s, with a 16-h light/8-h dark photoperiod.

Glasshouse conditions

Plant material was grown in the glasshouse to induce flowering for seed collection. Plants were grown in containers containing a 2 cm layer of 1:1 peat:sand mix, topped up with reverse osmosis water.

Seed sterilisation

Seeds were washed for 5 minutes in 70 % ethanol, 0.1 % SDS, washed in sterile water and transferred to 4% bleach, 0.2 % triton 100 for 10 minutes, then washed 3 times with sterile water.

Seed germination

Seeds were sown in sterilin jars containing a layer of solid culture medium (0.22 % MS, 2.5 % sucrose, 0.3 % agar, pH 5.8) topped up with liquid MS culture medium containing 0.1 mM ethephon (Sigma C0143). To make ethephon containing media, a concentrated 2.5 M ethephon solution was made in a pH 3 buffer (41 mM disodium hydrogen phosphate, 79 mM citric acid) and diluted in liquid media to a final concentration of 0.1 mM. Seedlings were germinated at 23 °C in CER conditions (as above). Once seeds had germinated, seedlings were removed from ethephon containing media and grown in MS liquid media (as above).

Mutagenesis of *U. gibba* tissue with EMS

U. gibba plants were grown in sterile culture prior to EMS treatment. Plant material was treated with 0.01 %, 0.05 %, 0.01 %, 0.15 %, 0.2 %, or 0.25 % EMS (ethyl methanesulfonate) diluted in 0.02 % tween 20 (Sigma-Aldrich, P9416). Tissue was incubated with the EMS solution while being continually agitated for 18 hours. Treated tissue was then passed through 10 x 20-minute washes in 0.02 % Tween, washed twice in water and incubated overnight in water and placed in the CER (as above). Tissue was divided into 441 separate M1 explants in the glasshouse (approximately 5 cm of stolon). Flowering M1 plants had seed collected to produce M2 generation to identify segregating phenotypes of interest to take on to M3. 30 different mutant phenotypes were recovered, included altered traps, absent traps, reduced leaf and stolon growth, long flower spurs, spiky leaves, multiple traps on leaves, and fasciation. For the family containing the dwarf and extreme-dwarf plants used in this study, phenotyping only separated plants into wild type, dwarf or extreme-dwarf plants, therefore subtleties in other segregating phenotypes may have been missed. All mutants are available on request.

Passaging *U. gibba*

Wild type, dwarf and extreme-dwarf plant material were treated in liquid culture using epibrassinolide (Sigma Aldrich, E1641) to provide exogenous brassinosteroid or brassinazole (Sigma Aldrich, SML 1406) to inhibit brassinosteroid biosynthesis. Newly grown plant material was sub-cultured into fresh media containing fresh treatment every week to ensure exposure level. Treated plant cultures were maintained in CER conditions described above.

Tracking stolons

2 cm length of dwarf plant stolon with an apex were isolated in sterilin jars for one week, imaged on a Leica M205C stereomicroscope with a Leica DFC495 camera (Leica, Milton Keynes, UK) at day 0 on a plate containing water, then again isolated in sterilin jars of liquid media containing the appropriate treatment and returned to CER. Individual stolons were imaged at day 7 then returned to fresh media containing the appropriate treatment for a week before being imaged at day 14. Individual images were stitched together in Adobe Photoshop and nodes labelled to identify internode 0 at day 0 and internodes and nodes which had subsequently appeared in treatment at day 14 were

labelled with negative numbers. Internode length measurements were made in ImageJ software (http://imagej.nih.gov/ij/).

A. thaliana plant material and growth

dwf4 seeds were purchased from Nottingham Arabidopsis Stock Centre, stock code (N839744).

Tissue culture

A. thaliana quasimodo2-1 plants were grown on plates containing MS media (0.441% Murashige and Skoog including vitamins, 1% (w/v) glucose, 0.05% (w/v) MES, 1% Difco agar, pH to 5.7). Sterilised seeds were stratified in the dark at 4°C for 2 days, then exposed for light for 4 hours at 20°C in a controlled environment room before being wrapped in three layers of tin foil to ensure etiolation. To inhibit BR, 1 µM of BRZ was chosen that has been shown to replicate the phenotype of a BR biosynthesis mutant (*32*). BRZ was added to media of treated seeds which were subjected to the same conditions and untreated seeds.

Seed sterilisation

Seeds were sterilised in 70% ethanol with 0.05% SDS for 5 minutes, followed by three washes in 100% ethanol. Seeds were air-dried on sterile filter paper before being plated (as above). If seeds were receiving hormonal treatment, then this was added to the media that the seeds would germinate on.

General methods

Propidium iodide staining for confocal imaging

The propidium iodide staining protocol for whole-mount imaging (*33*) was followed to stain *U. gibba* with the following extra steps. After the final water wash, tissue was mounted onto glass slides with added Frame-Seal Incubation Chambers (BIO-RAD, SLF0601). A drop of ½ strength chloral hydrate solution was added to cover the tissue and samples were incubated over-night at room temperature. Excess chloral hydrate was removed and samples correctly spaced on the cover slip. Samples were mounted in Hoyer's solution and a slide placed on top to ensure samples were close to the coverslip for imaging.

For single mutant *qua2-1, dwf4* and *qua2-1dwf4* double mutant hypocotyls were placed in 0.25 mg/ml propidium iodide for 10 minutes, washed in water then placed on a glass slide with added Frame-Seal Incubation Chambers (BIO-RAD, SLF0601) plus water before imaging.

Confocal imaging

Tissue samples were PI stained and mounted as described above. Imaging was performed using a x10 or x20 dry lens on a Zeiss 780 or 880, or Lecia SP8 confocal microscope. 561 nm excitation was used, collected at 625-690 nm.

Cell segmentation with MorphographX

Confocal Z-stacks were resized, brightness/contrast adjusted as required and converted to .tiff format with Image J (http://imagej.nih.gov/ij/). Stacks were loaded into MorphoGraphX open-source software (www.MorphoGraphX.org/Software/) and processes described in (*34*) followed to create surface meshes and segment epidermal cells. Heatmaps for cell area, max and min cell length, anisotropy (cell max length/ (cell max length + cell min length) and cell length parallel and perpendicular to a Bezier line drawn along the stolon axis were generated and data exported as .csv files and viewed in Microsoft Excel to generate charts.

VolViewer measurements

Confocal Z-stacks were imported into VolViewer (VolViewer - BanghamLab (uea.ac.uk) and measurements of stolon circumference and relative epidermal and vein length in chunks of stolon collected. VolViewer measurements are accurate to approximately ±5%

Statistical Analysis

Statistical analysis was performed using R version 2022.07.1. to perform ANOVA with Tukey post-hoc test in Fig. 2 D, I, J, fig. S2 A to D, fig. S6 G, N, U and fig. S8 E and F, and *t*-test in Fig. 4T and fig. S7 C.

Light microscopy imaging

Live plant tissues were imaged in water using a Leica M205C stereomicroscope with Leica DFC495 camera. Plant morphology phenotype measurements were taken using ImageJ software (http://imagej.nih.gov/ij/).

Transmission electron microscopy

Stolons and hypocotyls were cut into small pieces and immediately placed in a solution of 2.5% (v/v) glutaraldehyde in 0.05M sodium cacodylate, pH 7.3 for fixation, and left overnight at room temperature. When samples were too thin for the smallest Leica EM TP baskets they were embedded in 2% (v/v) low gelling temperature agarose in water and plunged into ice. Once the agarose had set, 1mm^3 blocks containing stolons or hypocotyls were cut out and placed in a solution of 2.5% (v/v) glutaraldehyde in 0.05M sodium cacodylate, pH 7.3 and left overnight to fix. The samples were loaded into a Leica EM TP embedding machine (Leica, Milton Keynes, UK) using the following protocol. The fixative was washed out by three successive 15-minute washes in 0.05M sodium cacodylate and post-fixed in 1% (w/v) OsO_4 in 0.05 M sodium cacodylate for one hour at room temperature. The osmium fixation was followed by three, 15-minute washes in distilled water before beginning the ethanol dehydration series (30%, 50%, 70%, 95% and two changes of 100% ethanol, each for an hour). Once dehydrated, samples were gradually infiltrated with LR White resin (London Resin Company, Reading, Berkshire) by successive changes of resin:ethanol mixes at room temperature (1:1 for 1hr, 2:1 for 1hr, 3:1 for 1hr, 100% resin for 1 hr then 100% resin for 16 hrs and a fresh change again for a further 8 hrs). Samples were transferred into gelatin capsules full of fresh LR White and placed at 60^{o}C for 16 hrs to polymerize. The material was sectioned with a diamond knife using a Leica UC7 ultramicrotome (Leica, Milton Keynes, UK) and ultrathin sections of approximately 90nm were picked up on 200 mesh copper grids which had been formvar and carbon coated (EM resolutions, Sheffield, UK). The sections were stained with 2% (w/v) uranyl acetate for 1hr and 1% (w/v) lead citrate for 1 minute, washed in distilled water and air dried. The grids were viewed in a FEI Talos 200C transmission electron microscope (FEI UK Ltd, Cambridge, UK) at 200kV and imaged using a Gatan OneView 4K x 4K digital camera (Gatan, Cambridge, UK) to record DM4 files. For the visualisation of the material by light microscopy, semi-thin sections of 500nm were taken using a Leica Artos 3D ultramicrotome, stained with 0.5% (w/v) Toluidine blue and imaged on a Zeiss Axio Imager Z2.

Freeze-fracture SEM

CryoSEM and cryofracture was carried out as described in (*35*) with the following modifications: (i) Iridium was used as the sputter coating target to a measured thickness of 3 nm and (ii) Imaging used the backscattered electron detector and a gun voltage of 25 kV and a probe current of 16 pA.

Determination of endogenous BRs levels

Cathasterone analysis was performed at JIC, UK with extraction of purification as described in (*36*) and instrumental analysis as in (*37*). Typhasterol, 6-deoxocastasterone, and castasterone were detected using deuterium-labelled standards at Institute of Genetics and Developmental Biology, China. The quantification of endogenous BRs levels was performed based on the method reported previously with some simplifications in sample pretreatment (*38*). 200 milligrams of the sample powder was extracted with 90% aqueous methanol (MeOH) in an ultrasonic bath for 1 hour. Simultaneously D_3-castasterone (CS), D_3-6-deoxocastasterone (6-deoxo-CS), and D_3-typhasterol (TY) were added to the extract as internal standards for BRs content measurement. After the MCX cartridge was activated and equilibrated with MeOH, water and 40% MeOH in sequence, the crude extracts reconstructed in 40% MeOH were loaded onto the cartridge. The MCX cartridge was washed with 40% MeOH, and then BRs eluted with MeOH. After drying with N_2 stream, the eluent was redissolved with ACN to be derivatized with 2-methoxypyridine-5-boronic acid (MPyBA) prior to UPLC-MS/MS analysis. BRs analysis was performed on a quadrupole linear ion trap hybrid MS (QTRAP 6500, AB SCIEX) equipped with an electrospray ionization source coupled with a UPLC (Waters) (*39*). As for CS, D_3-CS, 6-deoxo-CS, D_3-6-deoxo-CS, TY and D_3-TY, the MRM transition 582.4>178.1, 585.4>178.1, 568.4>178.1, 571.4>178.1, 566.4>548.3 and 569.4>548.3 was used for quantification.

Sequence Analysis

Genomic DNA from 11 mutants, 13 individuals displaying a wild-type phenotype were sequenced at the Chinese Academy of Science, Beijing to a minimum of 35x coverage. Sequence data for 72 biologically identical progenitor samples were pooled together to identify novel mutations that were introduced to the mutant family. Libraries were prepared using a TruSeq Nano DNA kit and sequencing performed on an Illumina Hiseq X Ten to produce 150bp paired-end reads. Reads were mapped using Burrows-Wheeler Aligner (bwa-0.7.17) to the Chromium 10x reference created from the progenitor. Quality filtering was done by removing read overlaps using clipOverlap (bamutil-1.0.14) and PCR duplicates using MarkDuplicates (picard-1.134) with the following settings: REMOVE_DUPLICATES = true ASSUME_SORTED = true VALIDATION_STRINGENCY = SILENT MAX_FILE_HANDLES_FOR_READ_ENDS_MAP = 900. Variable sites were called using HaplotypeCaller (GATK-4.0.9.0) to identify variable sites. Initial filtering was performed (BCFtools-1.8) for biallelic sites with a minimum allelic count of 1 using the following command: bcftools view -m 2 -M 2 -O v -c 1:minor and tabulated using VariantsToTable (GATK-4.0.9.0) with -GT command to output genotypes for each individual at each variable site. The candidate SNP was a C to T transition, consistent with being EMS-induced (*40*), and caused an early stop codon. The SNP was homozygous in all 12 mutants in the M2 family, and heterozygous or absent in all of the 33 wild type plants tested. The candidate gene was identified using the reference genome that has gene annotation (*41*). The coding sequence was extracted and annotated using Geneious (11.0.5).

Further genotyping was done using the KASP genotyping platform (LGC Genomics) using the VIC (5’-GAAGGTCGGAGTCAACGGATTAGGGGAGGAGCGGGCCTCGTGG-3’) and FAM (5’-GAAGGTGACCAAGTTCATGCTAGGGGAGGAGCGGGCCTCGTGA-3’) fluorescent probes and a common reverse primer (5’- GTAGCTGCTTCTCGACGGCTCC-3’).

Supplementary Text

Tissue-level Modelling

All models were creating using GFtbox (https://coensoft.jic.ac.uk/software) and deposited at Github: https://github.com/JIC-Enrico-Coen/Cell_Layer_Interactions_2023.

Utricularia tissue-level models (Fig. 4 A to R, fig. S4)

An initial mesh was created with an outer cylinder (epidermis) connected through six blades to an axial core (fig. S10A, B). The epidermis was set to be twice as stiff as internal regions because of the greater thickness of the outer epidermal wall. Different regions of the mesh express different identity factors: EPIDERMIS, BLADES, and AXIS. Polarity initially ran from base to top of the cylinder and then deformed with the tissue. Specified growth was only parallel to the polarity and set to 4% per time unit for all regions in the wild-type model, and set to zero for EPIDERMIS in the dwarf mutant model. To reduce boundary effects, stolon ends were constrained to remain in the horizontal plane. To prevent tissue stresses generated at each time step from accumulating indefinitely, accumulated tissue stress decayed at a rate of 50% per time step, corresponding to the process of stress relaxation (*42*). At the start, the mesh was given a small random perturbation to the positions of all the vertexes, to break the symmetry and allow buckling. All models were run for the same number of time units, except for the model in which the middle third of the blades were missing, which was run for half the time to avoid excessive buckling.

Limitations of Utricularia tissue-level model

The model assumes the growth constraint comes from slower specified growth of the epidermis, whereas in real tissue the constraint may come mainly from the outer wall of the epidermis. The models do not have collision detection, so the insides can penetrate the outsides if models are run for too long (e.g. model in which one third of the blades are absent).

Arabidopsis tissue-level models (Fig. 5 F to I)

An initial solid mesh was created as 6 concentric cylinders of finite elements (fig. S10C). The outer cylinder was assigned EPIDERMIS identity and the rest INNER identity (cyan). The surface-half of the EPIDERMIS region was colored purple and the internal half cyan. The bulk modulus of the EPIDERMIS region was four times that of the inner region, reflecting the greater average wall thickness of the hypocotyl epidermis (fig. S8). Polarity initially ran from base to top of the cylinder and then deformed with the tissue. Specified growth was only parallel to the polarity. For the control model (Fig. 5G), all regions had the same growth rate (4% per time step). For the dwarf model (Fig. 5H and I), specified growth rate of the EPIDERMIS region was set to 0, while that of the INNER region remained at 4%.

Cracks formed along boundaries of the finite elements when the tissue stress exceeded a threshold level. To prevent the tissue all cracking at once, variation in weakness was generated in the mesh. A diffusible factor, WEAKNESS, was initially given an independent random value at every vertex. WEAKNESS set the strength of the tissue: the higher the value, the lower the tension at which it would crack. WEAKNESS was always in the range from 0 to the 'weakness' parameter. The distribution of WEAKNESS was smoothened by diffusion for the time specified by 'diffusiontime', before growth initiated. After each diffusion step, WEAKNESS was rescaled to the interval from 0 to 'weakness'. After that time, its diffusivity was set to zero to freeze the pattern, and growth started. The parameter 'breakingstress' defined the tissue stress required to make or extend a crack. To prevent tissue stresses generated at each time step from accumulating indefinitely, accumulated tissue stress decayed at a rate of 50% per time step, corresponding to the process of stress relaxation (*42*). All models were run for the same number of time units.

Limitations of Arabidopsis tissue-level model

The direction of the cracks is biased by the structure of the mesh, because the implementation of cracks only allows them to form along the boundaries of the finite elements. In real tissue, the pattern of cracks would follow the lines of weakness between cells, a feature not incorporated in the model. Also, weak adhesion between epidermal and subepidermal layers is not incorporated in the model, so cracks cannot open up through epidermis peeling away from the subepidermis.

Cell-level modelling (Fig. 5, J to V)

Models are deposited at Github:

https://github.com/JIC-Enrico-Coen/Cell_Layer_Interactions_2023.

Cellular template creation

The cellular template for the simulation model was created in CellMaker, an addon for the MorphoDynamX software (www.MorphoDynamX.org). A 2D grid of 37 hexagonal cells approximately 300 μm^2 in area was generated and the cells rounded on the edges to better estimate the shape of a hypocotyl cross section (fig. S10 E). This template was then extruded into a cylinder of 321 3D cells with adjacent cells and layers staggered. The template was then triangulated to give a mesh with triangles approximately 5 μm^2 in area and just over 40,000 triangles. The cross section was that of a smoothed hexagon, and cross-sectional areas of cells were within 0.02% of each other (fig. S10 F). Epidermal corner cells were slightly smaller in cross-sectional area and had a greater proportion outer wall to inner wall than other epidermal cells.

Modelling creep

We assume cellulose microfibrils are the major load-bearing components of the wall (*22*). For an individual microfibril, microfibril stress, σ_f, and elastic microfibril strain, ε_e, and microfibril strain are related by equation:

(1) $\sigma_f = \varepsilon_e E_f$

where E_f is the Young's modulus of the microfibril. Creep arises through irreversible slippage of microfibrils. In a simple linear case, slippage or creep rate, $\dot{\varepsilon}_c$, can be related to fibre stress according to the Lockhart equation (*43*):

(2) $\dot{\varepsilon}_c = \varphi(\sigma_f - \sigma_Y)$, where φ is the extensibility and σ_Y the yield threshold.

Substituting (1) into (2) we have:

(3) $\dot{\varepsilon}_c = \varphi(\varepsilon_e E_f, - \sigma_Y)$,

Or

(4) $\dot{\varepsilon}_c = \varphi E_f (\varepsilon_e - \sigma_Y / E_f)$

Thus, creep rate is proportional to how much the elastic fibre strain exceeds a threshold strain σ_Y / E_f. When considering a wall comprising multiple microfibrils, elastic wall strain in a given direction should be the same as elastic fibre strain in that direction. Similarly, wall creep rate should be the same fibre creep rate. Assuming that the Young's modulus of microfibrils is constant, we can then express wall creep rate as:

(5) $\dot{\varepsilon}_c = \varphi_w (\varepsilon_e - \varepsilon_{yw})$

Where φ_w, is wall extensibility (equal to φE_f) and ε_{yw} is threshold wall strain (equal to σ_Y / E_f). For a small time step Δt, we assume φ_w is less than 1. Thus, the amount of creep is a fraction of the elastic strain in excess of the threshold ε_{yw}:

(6) $\Delta\varepsilon_c = \varphi_w (\varepsilon_e - \varepsilon_{yw})$

The value of ε_e will be inversely proportional to the number of microfibrils resisting tensile force in a cross section of wall, which will depend on wall thickness and wall anisotropy (the proportion of microfibrils oriented in the direction parallel to the tensile force). Dirichlet conditions fixed all degrees of freedom of a central vertex. Vertices on the central XZ plane were fixed in the Y direction for all cell layers except the leftmost two where the cracks occur. Note that the simulation is almost symmetric about this plane, save for small differences in cell staggering.

Finite element implementation of creep

The FEM simulation was performed using the MorphoMechanX (www.MorphoMechanX.org) software, an addon for MorphoDynamX for finite element mechanical simulation. Triangle elements of 3D cells were assigned a St. Venant transverse isotropic (*44, 45*) with a Youngs modulus of 150 MPa in the longitudinal (vertical) direction and 1050 MPa in the transverse (horizontal) direction. The cells were pressurized with uniform turgor pressure of 0.5 MPa with the Poission’s ratio equivalent set to 0.3 (*45*). See Table S2 for simulation parameters that differed between the genotypes. Implementation of equation (6) followed that of (*46*), updated to use an anisotropic material (*47*), with $\Delta\varepsilon_c$ in each direction implemented by changing the reference configuration of individual elements by the appropriate amount.

We assumed mean wall stiffness depended on two components: matrix which contributed a small proportion of overall stiffness, and microfibrils, which contributed most stiffness. The matrix contribution was assumed to be isotropic whereas microfibril contribution was anisotropic. The longitudinal axis of a cell was initially oriented vertically, but rotated with the tissue if it curved (i.e. at a crack). We assume matrix contributed an amount *x* to the

Young's modulus of the wall in all directions, microfibrils 2*x* parallel to the longitudinal axis, and 20*x* perpendicular to the longitudinal axis, giving an overall anisotropy in the Young's modulus of 7:1 (21*x*:3*x*).

Crack formation

To simulate crack formation, fracture vertices were selected at the junctions between epidermal cells and nearby junctions with subepidermal cells. The fractures were 2 epidermal cells wide for the *qua2* single mutant, and 8 cells wide for *qua2 dwf4*. At a specified time in the simulation, the vertices were separated by duplicating vertices, edges, and faces, propagating all values for the material parameters, pressure and the reference configuration. Upon fracturing, free epidermal cell ends rounded up due to release from mechanical constraint. With further growth, the fracture opened, with the separated ends of the 3D cells free to grow and expand independently (Movie 2). Opening required fracture vertices to incorporate epidermal-subepidermal junctions, which may reflect weak epidermal-subepidermal cell adhesion, further weakened by the *qua2* mutation. No attempt was made to reconcile collision detection, so the cells could interpenetrate slightly after separation due to bulging from turgor.

Visualization of stresses and growth rates

The visualization of tissue stress displayed the difference between the longitudinal stress due to turgor within a cell when grown in mechanical isolation (cell-autonomous stress), and the resultant longitudinal stress over that cell when embedded in the tissue, which arises from the cell's turgor plus connectivity between cells.

To calculate the average resultant longitudinal stress of a cell, first a longitudinal axis for each 3D cell was determined by averaging stiffness orientations for all the triangles belonging to that cell. This longitudinal axis was vertical initially but may change slightly as it deformed with the cells (e.g. where cracks form). A cross section of the cell was then taken perpendicular to this average longitudinal axis through the centroid of the cell. The stress component along this axis was then averaged for all the triangles that fall on this cross section, weighted by the wall area on the section for each triangle. This gave the average resultant longitudinal stress in the simulation for the cell. Longitudinal stresses were not calculated on cross walls and were set to zero.

The cell-autonomous longitudinal stress of a cell is calculated by growing a cell with the same material properties in mechanical isolation from other cells and calculating its average wall stresses, by taking the area of the cross section multiplied by the turgor pressure, and dividing by the total area of the wall on the cross section. The difference between the resultant longitudinal stress and the cell-autonomous stress is the tissue stress. Cell-cell adhesion causes walls to flatten, reducing wall tension slightly and putting the adhesive (middle lamella) under tension.

Specified growth rate was determined by calculating the growth rate of a cell in mechanical isolation from the extensibility multiplied by its longitudinal strain rate. Dirichlet conditions limiting the movement of the two vertices in the centre of the end faces in the transverse directions prevented the cell from bending for epidermal cells where a portion of the walls are thicker. Since there was some variation in epidermal cells, some having 3 external faces and some 2, specified growth for epidermal cells was determined from the average.

Limitations of the model

To reduce the time required to run the simulation, a structure similar in shape to a hypocotyl was used, but with fewer internal cells. This changed the ratio between the inner and outer tissue, and would underestimate tissue stresses. Tissue stress visualization was also limited, as the orientation approximation for highly curved cells is inaccurate. For this reason, tissue stress was set zero for separated cells. The tissue stress calculation aims to visualize how the stresses in the epidermal layer compare to the inner tissue stresses. However, this approximation can cause artifacts since it is based on an average (not all walls are the same thickness). In contrast to the tissue-level model, a crack was introduced at a specific location not dependent on stress, and it extended to the epidermal-subepidermal interface. Although it would be possible for the location of cracks to be emergent in the model (i.e dependant on stress levels), it would require the simulation of a great many more cells. The triangle size was also chosen to be as coarse as possible to reduce simulation time. Another model limitation is the lack of collision detection. After cracking, cells would bulge slightly into each other due to turgor pressure, an effect that was exaggerated by growth.

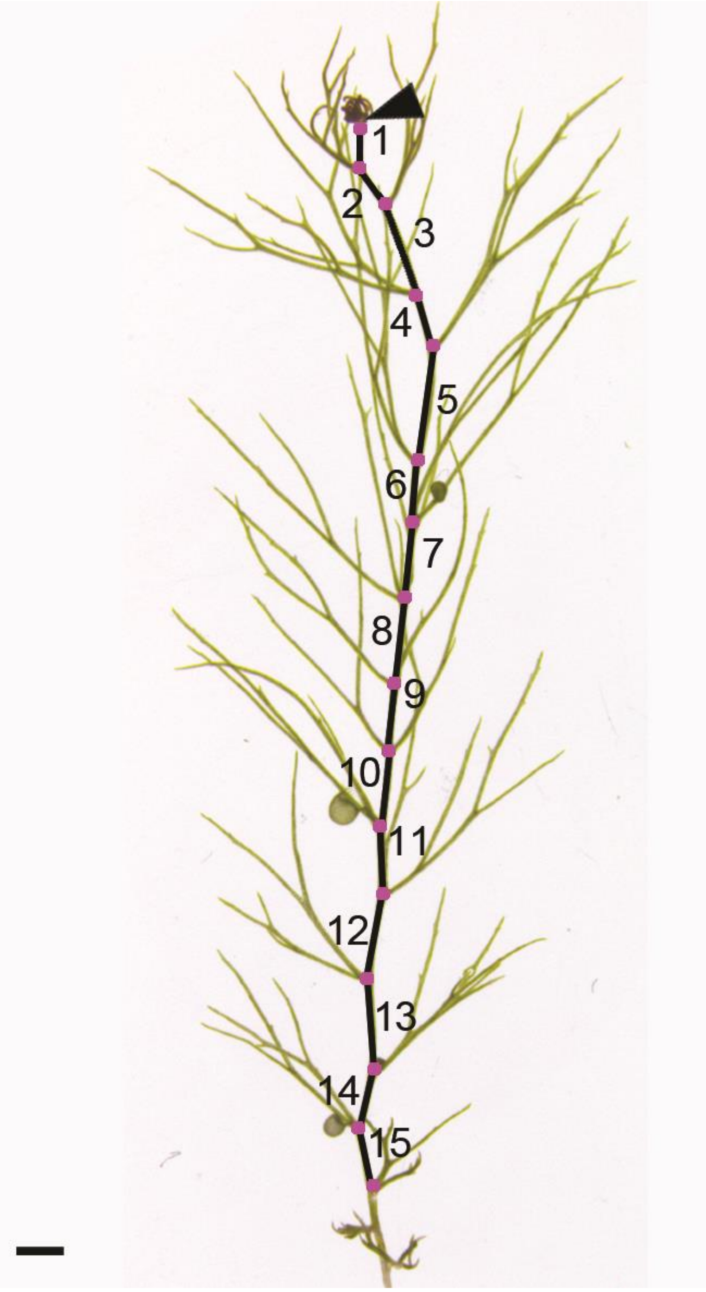

Fig. S1. Internode numbers increase with stolon maturity

Black arrowhead indicates first fully emerged leaf from apex, used to identify the beginning of internode 1. Nodes shown with magenta dots. Scale bar 1 mm.

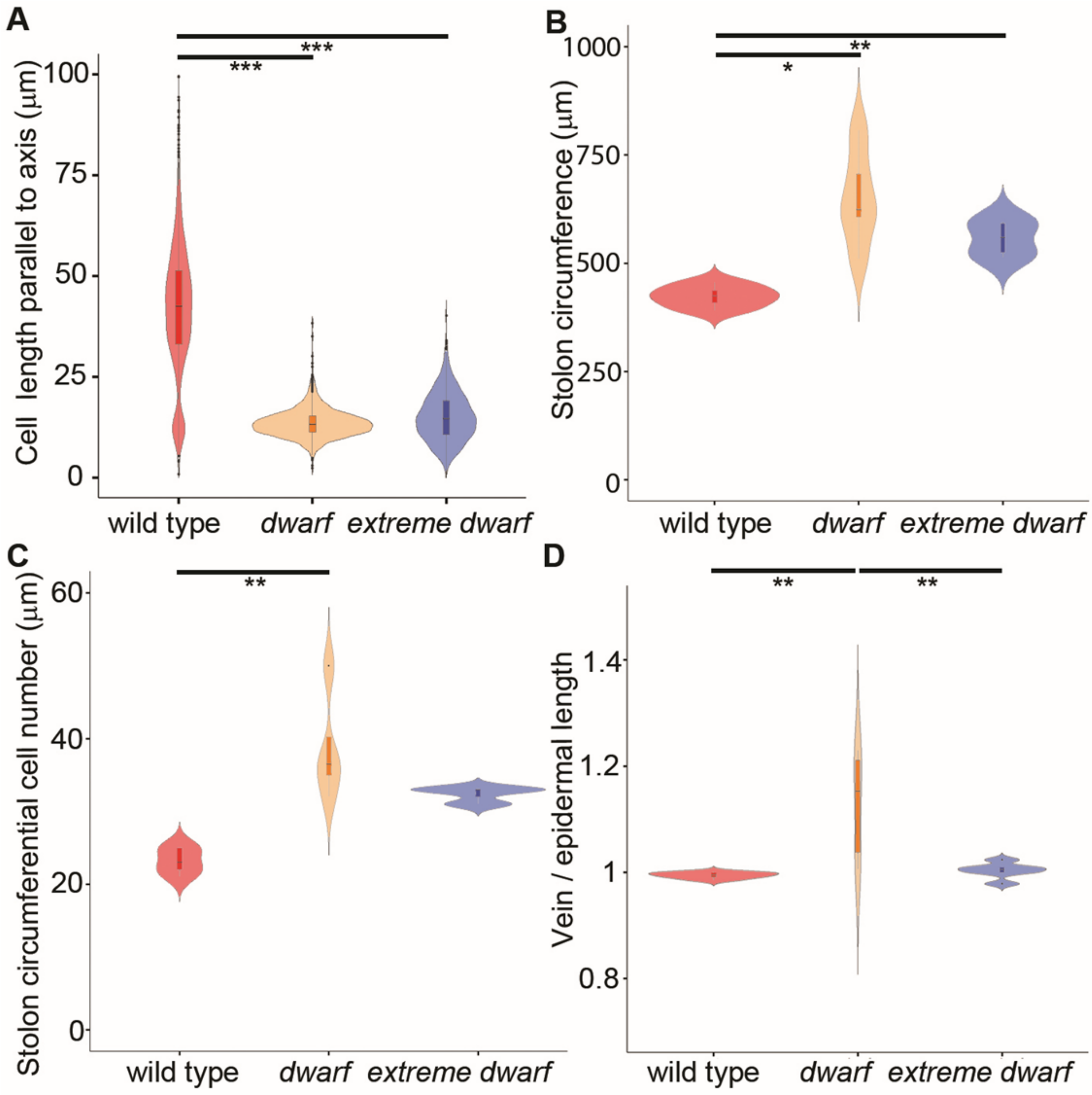

Fig. S2. Charts comparing U. gibba wild type, *dwarf* and *extreme dwarf* stolon circumference, cell number, cell length and vein to epidermal length ratio

(**A**) Cell length parallel to stolon axis of mature stolons of wild type (n=1817 cells from 8 plants), dwarf (n=2289 cells from 5 plants) and extreme-dwarf (n=1494 cells from 4 plants). Both mutants have significantly lower values than wild type ($p< 0.001$ ***). Epidermal cells were segmented in MorphographX and axial cell length obtained in relation to a manually placed Bezier line which ran the length of the stolon. Mean cell length parallel to the axis is 41.5 µm +/- 1.71 (SEM) for wild type, 13.5 µm +/- 0.64 (SEM) for dwarf, and 15.1 µm +/- 1.62 (SEM) for extreme-dwarf, showing axial cell length in dwarf mutants is reduced by a factor of 3, and extreme-dwarf a factor of 2.7. By comparison, mean internode length was 3.07 mm +/- 0.11 (SEM) for wild type, 0.72 mm +/- 0.02 (SEM) for dwarf and 0.29 mm +/- 0.01 (SEM) for extreme-dwarf (Fig. 2D), indicating dwarf internode length is reduced by a factor of 4.25, and extreme-dwarf by a factor of 10.5. These findings suggest that about 70% (3/4.25) of the reduction of dwarf internode length, and 26% (2.7/10.5) of the reduction of extreme-dwarf internode length were caused by reduced cell length, with the remaining reduction caused by reduced cell number. (**B**) Stolon circumference from transverse section of wild type (n=5), dwarf (n=5) and extreme-dwarf (n=4). Both dwarf ($p<0.01$ **) and extreme-dwarf ($p<0.05$ *) have greater circumference than wild type. (**C**) Stolon circumferential cell number from transverse section of wild type (n=5), dwarf (n=4) and extreme-dwarf (n=3). Dwarf ($p<0.01$ **) had a significantly greater number of cells than wild type. Together these data show that dwarf has a 54% greater circumferential length and a 70% increase in circumferential cell number, and the extreme mutant has a 32% greater circumferential length and a 39% increase in circumferential cell number than wild type, suggesting an increase in radial and circumferential growth prior to division arrest in the absence of brassinosteroid.

(**D**) Ratios of vascular length, V, to epidermal length, E (V/E) of wild type (n=6), dwarf (n=5) and extreme-dwarf (n=6). Dwarf had a significantly higher ratio than both wild type and extreme dwarf ($p<0.01$ **). Stolon circumferences were measured with a line encircling a transverse clip of the stolon volume at the surface of the epidermis in VolViewer. Cells were counted by placing points at cell centres within the circumference line. Vascular and epidermal lengths were obtained by placing measurement lines in a clipped chunk of the stolon volume in VolViewer.

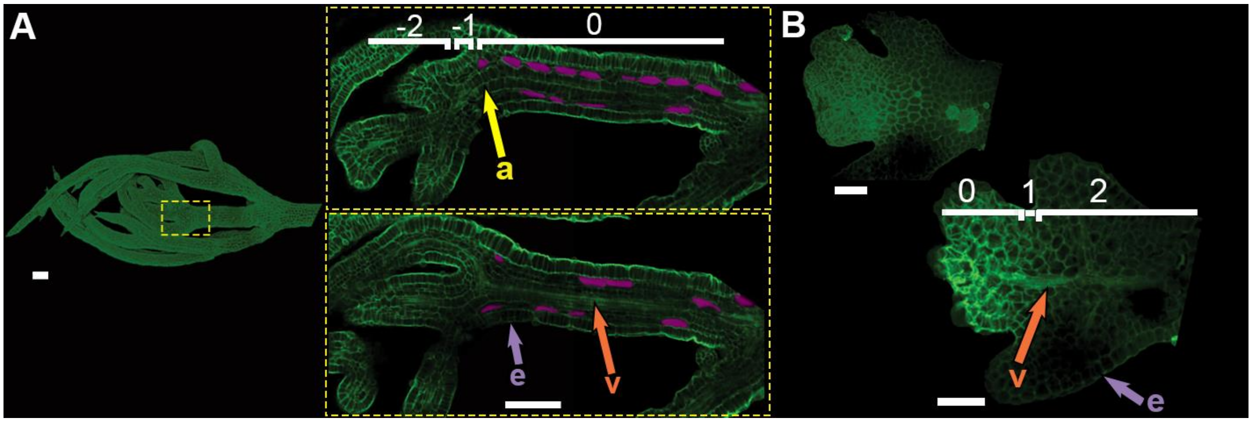

Fig. S3. Wild type and *extreme dwarf* inner tissue organization at early stages

(A) Confocal scan projection of early wild type internodes. Yellow rectangle highlights an enlarged region of the stolon with longitudinal slices taken above the vein (top) and around the vein (bottom). Air spaces are coloured in magenta. Breaking up of air spaces may be caused by variation in blade thickness.

(B) Confocal scan projection of early extreme dwarf internodes (upper left). Zoomed in longitudinal section below shows vein but no air spaces.

Axial core cells (yellow arrow), vasculature (orange arrow), epidermis (purple arrow). Internodes correspond to the numbered lines. Scale bars 100 µm.

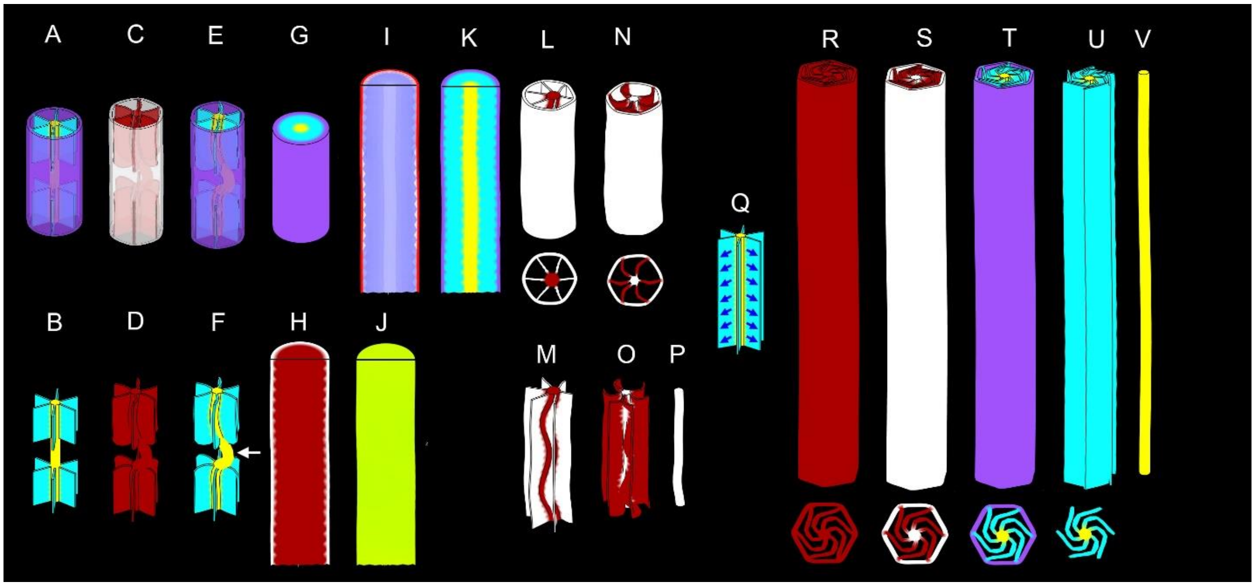

Fig S4. Simulations of growth models for Utricularia

(**A**-**F**) Model in which blades have been removed from the middle third of the cylinder. (A) Initial state - epidermis (purple), blades (cyan) and axial core (yellow). Tissue is partially transparent to allow internal structure to be seen. (B) as (A) without epidermis. (C) Exclusion of high specified growth (red) from epidermis gives a short cylinder with twisted blades and core. This simulation was run for half the length of time to those in Fig. 4 and the other models of this figure to avoid excessive buckling of the core. (D) As C without epidermis. (E) As (D) but color-coded for tissue. (F) As (E) without epidermis. Arrow points to buckled core. (**G** to **K**) Model with solid cylinder instead of blades with air spaces. (G) Initial state. (H) Longitudinal section at end of simulation showing specified growth rate (high (red) except in epidermis (white)). (I) As (H) but color-coded for tissue stresses (scale as in Fig. 4R). (J) As (H) but color-coded for resultant longitudinal growth rate (scale as in Fig. 4Q). (K) As (H) but color-coded for tissue, showing straight axial core. (**L** and **M**) Model with high specified growth rate only in the core. (I) Side view with transverse slice shown below. (J) As (I) with epidermis clipped away. (**N** to **P**) Model with high specified growth rate only in blades. (N) Oblique side view with transverse slice shown below. (O) As (N) with epidermis clipped away. (P) As (N) with both epidermis and blades clipped away. (**Q** to **V**) Model with radial growth of blades. (Q) Initial state with epidermis clipped away to reveal radial polarity field (arrows), which is present in addition to the vertical polarity field (Fig. 4A). (R) Final state color-coded for specified growth rate parallel to the vertical polarity field, with transverse slice below. (S) Final state color-coded for specified growth rate parallel to the radial polarity field, with transverse slice below. (T) Final state color-coded for tissue type, with transverse slice below. (U) As (T), with epidermis clipped away. (V) As (U) with blades clipped away.

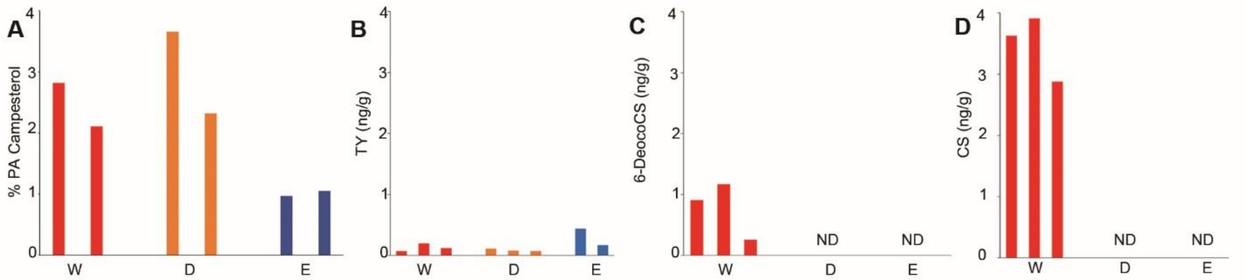

Fig. S5. Brassinosteroid precursors in dwarf plants of *U. gibba*

(**A**) Level of Campesterol, a BR precursor upstream of the *dwarf4* block in *Arabidopsis*. As no internal standard was available for Campesterol, the level of Campesterol was calculated by the percentage of the chromatogram area occupied by its peak. Replicates shown for different individuals. (**B-D**) Levels of precursors downstream of the *dwarf4* block. (B) Typhasterol (TY), (C) 6-Deoxocastasterone (6-DeoxoCS) and (D) Castasterone (CS) in ng/g of tissue. TY is present in all samples but at low levels and therefore could be attributed to noise. Precursors are shown from left to right in their position on the biosynthetic pathway (*48*). Wild type (W, red), dwarf (D, orange) and extreme-dwarf (E, blue). ND = not detected.

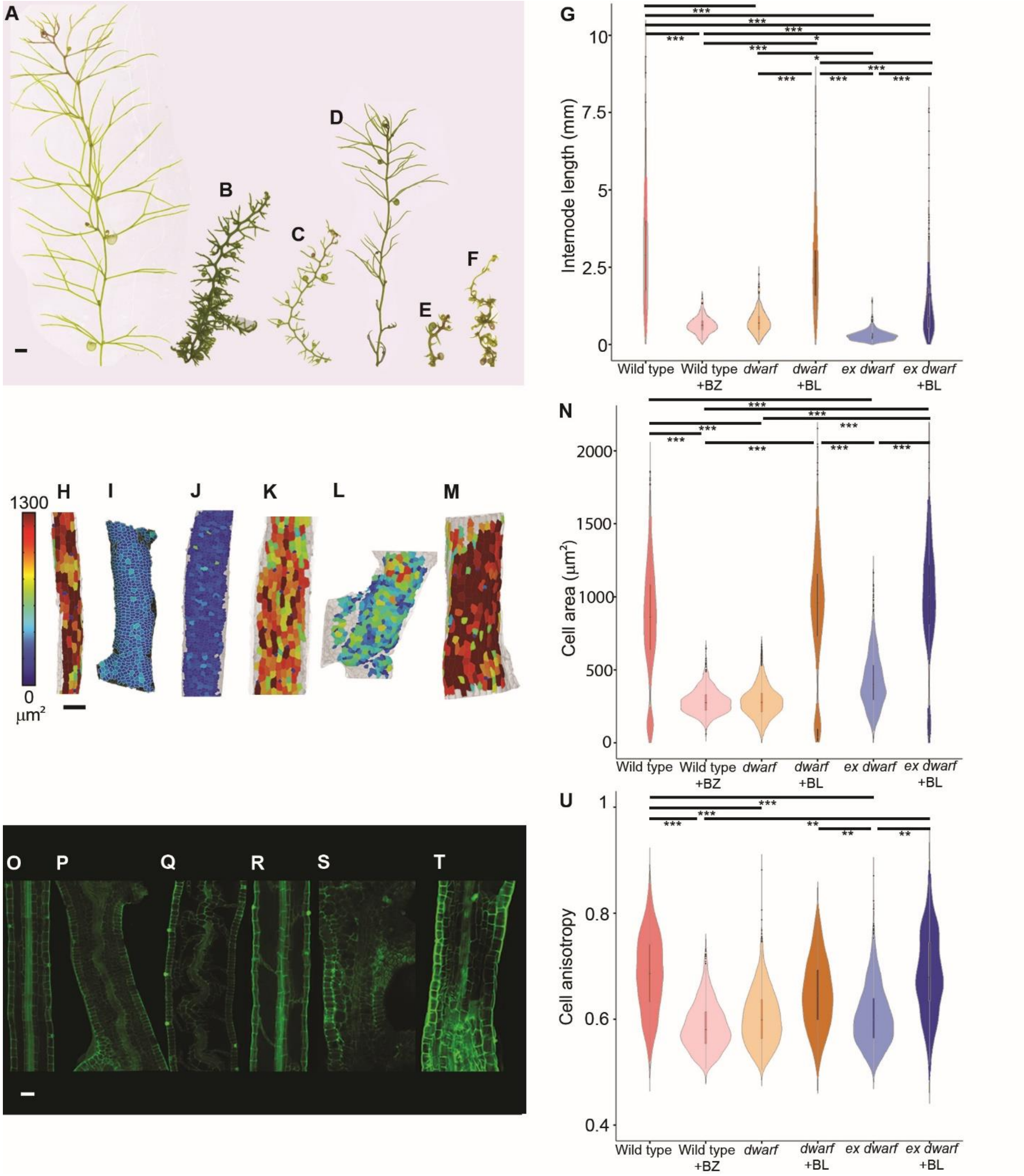
A
B
C
D
E
F
G
Internode length (mm)
10
7.5
5
2.5
0
Wild type
Wild type +BZ
dwarf
dwarf +BL
ex dwarf
ex dwarf +BL
***
*
1300
0
µm²
H
I
J
K
L
M
N
Cell area (µm²)
2000
1500
1000
500
0
O
P
Q
R
S
T
U
Cell anisotropy
1
0.8
0.6
0.4
**

Fig. S6. Treating with brassinolide rescues dwarf, and partially rescues extreme-dwarf while inhibiting brassinosteroid biosynthesis in wild type replicates the dwarf phenotype

(**A** to **F**) Whole-plant phenotypes. (A) Wild type. (B) Wild type + 0.5 µM BRZ. (C) Dwarf. (D) Dwarf + 0.01 uM epiBL. (E) Extreme-dwarf. (F) Extreme-dwarf + 0.01 uM epiBL. Scale bar 1 mm. (**G**) Violin plots of mature internode lengths of wild-type (n=10, as in Fig. 2D), Wild type + 0.5 µM BRZ (n=7), dwarf (n=10, as in Fig. 2D) dwarf + 0.01 uM epiBL (n=19), extreme-dwarf (n=13, as in Fig. 2D) and extreme-dwarf + 0.01 uM epiBL (n=15). Plants were grown in continuous culture. Block indicates interquartile range and horizontal line the mean. Both treated mutants had greater lengths than untreated ($p < 0.001$ ***). Dwarf + 0.01 uM epiBL was not significantly different from wild type (p = 0.768). Wild type treated with BRZ brassinosteroid inhibitor had significantly shorter stolons ($p < 0.001$ ***). (**H** to **M**) Heat maps of cell area in mature stolons. Epidermal cells were segmented in MorphographX and cell area obtained. (H) Wild type. (I) Wild type + 0.5 µM BRZ. (J) Dwarf. (K) Dwarf + 0.01 uM epiBL. (L) Extreme-dwarf. (M) Extreme-dwarf + 0.01 uM epiBL. Scale bar 100mm. (**N** and **U**) Violin plots of cell area (N) and cell anisotropy (cell max length/(cell max length + cell min length)) (U) of mature stolons of wild type (n=1817 cells from 8 plants, as in Fig.2 I and J), Wild type + 0.5 µM BRZ (wt + BRZ n = 1104 cells from 2 plants), dwarf (n=2289 cells from 5 plants, as in Fig.2 I and J), dwarf + 0.01 uM epiBL (n=721 cells from 3 plants), extreme-dwarf (n=1494 cells from 4 plants, as in Fig. 2 I and J) and extreme-dwarf + 0.01 uM epiBL (n =327 cells from 2 plants). Epidermal cells from confocal scans were segmented in MorphographX and cell area and anisotropy obtained. Both treated mutants had increased lengths compared untreated ($p < 0.001$ ***, L; $p < 0.01$ **, R). Both dwarf + 0.01 uM epiBL and ex dwarf + 0.01 uM epiBL were not significantly different to wild type cell area (p =0.99 for dwarf+BL and p=0.30 for ex+BL) and cell anisotropy (p =0.34 for dwarf+BL and p=0.99 for ex+BL). Wild type treated with BRZ brassinosteroid inhibitor had significantly shorter cells ($p < 0.001$ ***). **(O to T)** Longitudinal confocal sections. (O) Wild type. (P) Wild type + 0.5 µM BRZ. (Q) Dwarf. (R) Dwarf + 0.01 uM epiBL. (S) Extreme-dwarf. (T) Extreme-dwarf + 0.01 uM epiBL. Scale bar 50 µm.

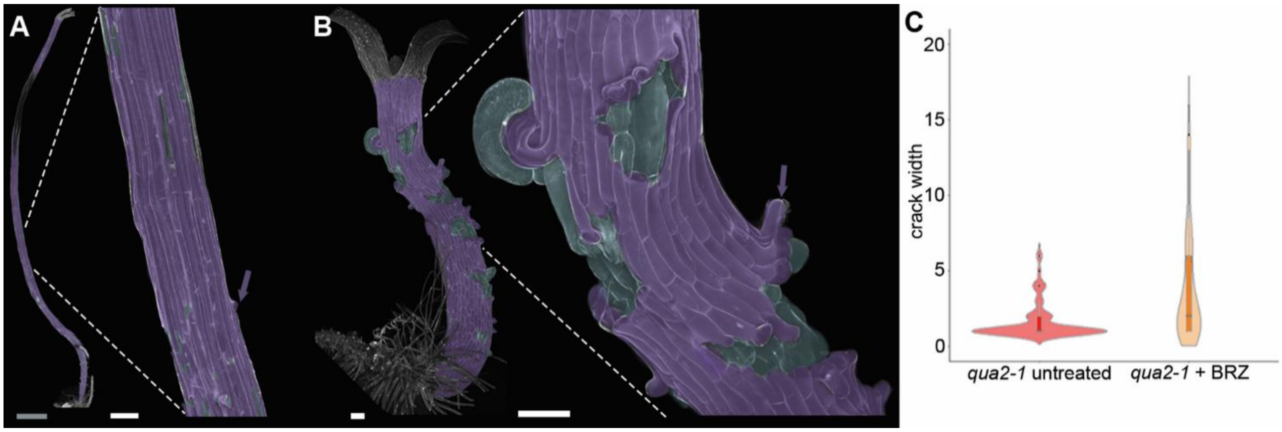

Fig. S7 Phenotype of *qua2-1* Arabidopsis hypocotyls treated with brassinosteroid inhibitor.

(**A** to **B**) Confocal images of seedlings after 9 days growth in dark. (A) *qua2-1* with close up of a region with cracks selected for magnification (B) *qua2-1* grown on 1 µM brassinazole with close up. Curved cells at crack boundaries are arrowed; epidermis cells (purple), internal cells (cyan). Scale bars 100 µm except A (grey) which is 1000µm (**C**) Violin plots of crack widths. Mean crack width covers more cell files in *qua2-1* + BRZ ($\bar{x}$ = 4.089 +/- 0.38 (SEM)) than *qua2-1* untreated ($\bar{x}$ = 1.611 +/- 0.14 (SEM)), but not significantly greater ($p = 0.0531$, untreated hypocotyls n = 2, n cracks = 74, brassinazole-treated hypocotyls n = 6, n cracks = 83).

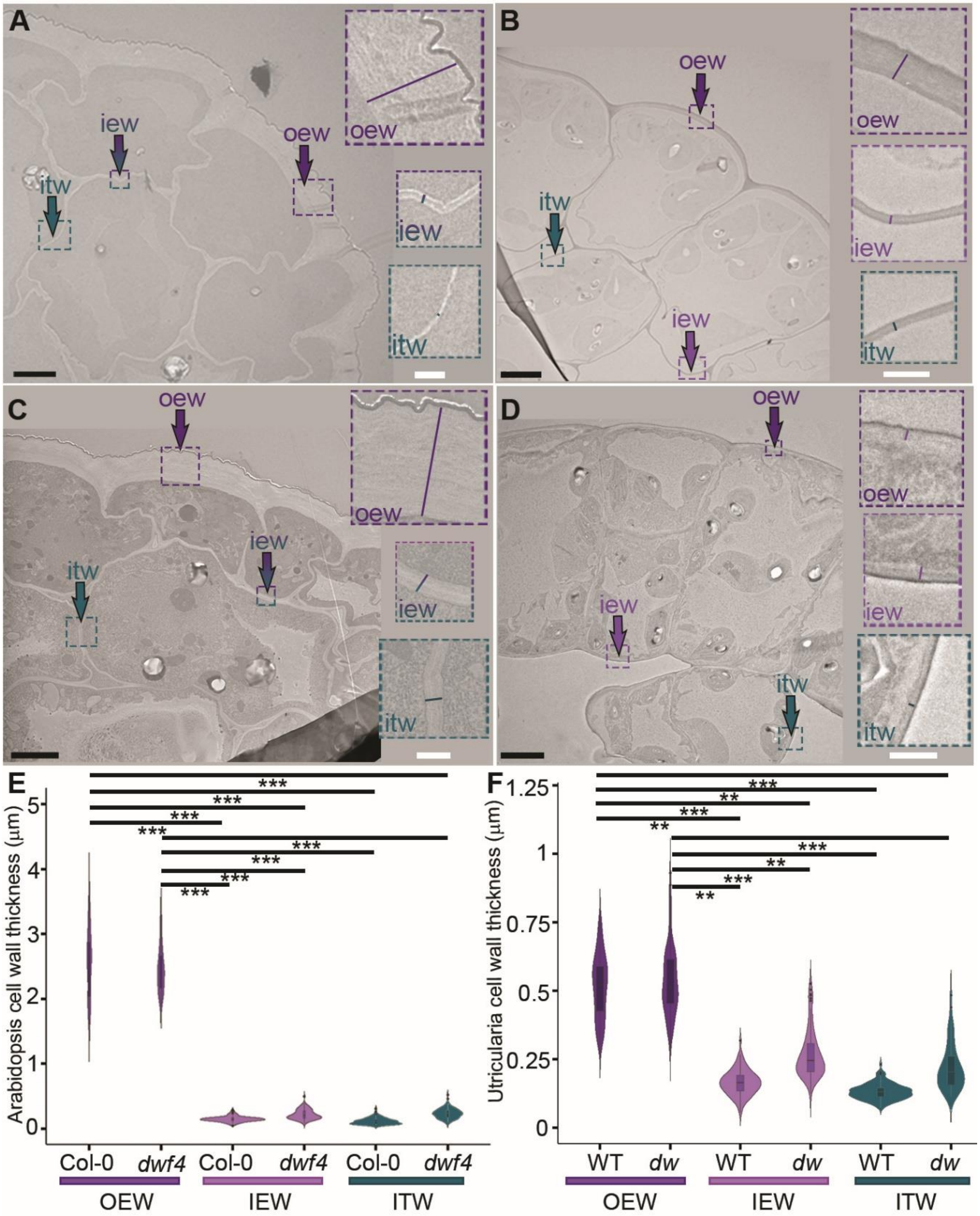
A
iew
oew
itw
oew
iew
itw
B
oew
itw
iew
oew
iew
itw
C
oew
iew
itw
oew
iew
itw
D
oew
iew
itw
oew
iew
itw
E
Arabidopsis cell wall thickness (μm)
0
1
2
3
4
5
***
***
***
***
***
***
***
***
Col-0
dwf4
Col-0
dwf4
Col-0
dwf4
OEW
IEW
ITW
F
Utricularia cell wall thickness (μm)
0
0.25
0.5
0.75
1
1.25
***
**
***
**
***
**
***
**
WT
dw
WT
dw
WT
dw
OEW
IEW
ITW

Fig. S8 Outer epidermal walls are thicker than internal cells and mutant inner walls are thicker than wild type in both *Arabidopsis* and *Utricularia* at early stages.

(**A** to **D**) Transmission electron micrographs of transverse sections showing outer epidermal wall (OEW, purple arrow and boxes for zoom), inner epidermal wall (IEW, lilac to cyan arrow and boxes for zoom) and inner tissue cell walls (ITW, cyan arrowheads and boxes for zoom). (A) Arabidopsis wild type (Col-0) hypocotyl after 4 days growth, showing thicker outer epidermal cell wall. (B) Wild type *U. gibba* internode 1. (C) Arabidopsis dwf4 mutant hypocotyl after 4 days growth, showing thicker outer epidermal cell wall. (D) dwarf mutant *U. gibba* internode 1. Scale bars 5 µm. (**E**) Arabidopsis violin plots of average cell wall thickness of Col-0 OEW ($\bar{x}$ = 2.56 +/- 0.06 (SEM) µm, n = 76 from 3 plants), IEW ($\bar{x}$ = 0.15 µm +/- 0.01 (SEM), n = 126 from 3 plants) and IT ($\bar{x}$ = 0.11 µm +/- 0.01 (SEM), n = 90 from 3 plants) and *dwf4* OEW ($\bar{x}$ = 2.45 µm +/- 0.04 (SEM), n = 92 from 3 plants), IEW ($\bar{x}$ = 0.22 µm +/- 0.01 (SEM), n = 136 from 3 plants) and IT ($\bar{x}$ = 0.23 µm +/- 0.01 (SEM), n = 123 from 3 plants). Block indicates interquartile range and horizontal line the mean. OEW is greater than both inner epidermal walls and inner tissue walls ($p < 0.001$). (**F**) *U. gibba* violin plots of average cell wall thickness of wild type OEW ($\bar{x}$ = 0.52 µm +/- 0.01 (SEM), n = 103 from 3 plants), IEW ($\bar{x}$ = 0.16 µm +/- 0.01 (SEM), n = 84 from 3 plants) and IT ($\bar{x}$ = 0.13 µm +/- 0.01 (SEM), n = 109 from 3 plants) and dwarf OEW ($\bar{x}$ = 0.54 µm +/- 0.01 (SEM), n = 105 from 3 plants), IEW ($\bar{x}$ = 0.27 µm +/- 0.01 (SEM), n = 81 from 3 plants) and IT ($\bar{x}$ = 0.22 µm +/- 0.01 (SEM), n = 63 from 3 plants). Block indicates interquartile range and horizontal line the mean. OEW is greater than both inner epidermal walls and inner tissue walls ($p < 0.001$ ***).

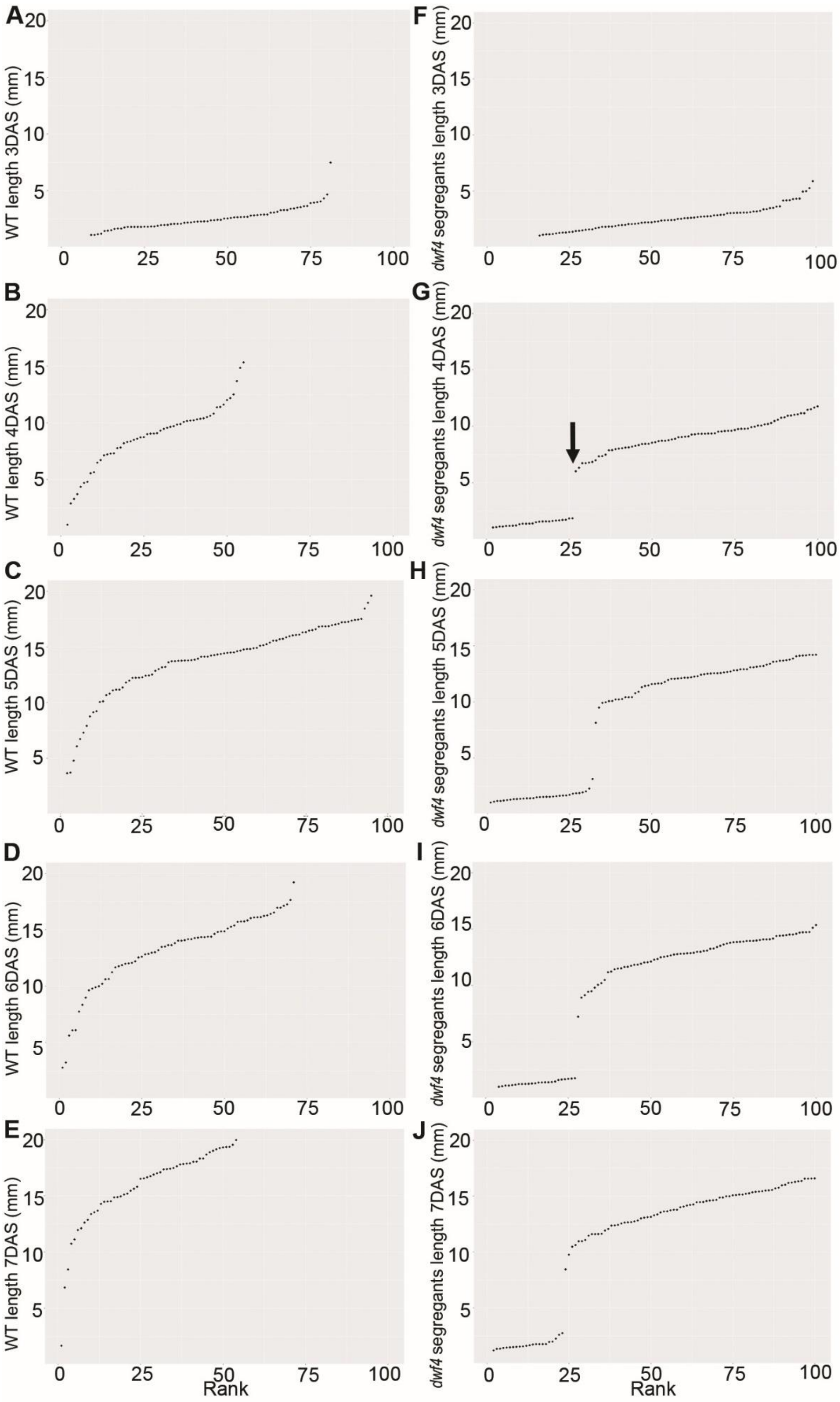
A
WT length 3DAS (mm)
B
WT length 4DAS (mm)
C
WT length 5DAS (mm)
D
WT length 6DAS (mm)
E
WT length 7DAS (mm)
F
dwf4 segregants length 3DAS (mm)
G
dwf4 segregants length 4DAS (mm)
H
dwf4 segregants length 5DAS (mm)
I
dwf4 segregants length 6DAS (mm)
J
dwf4 segregants length 7DAS (mm)
5
10
15
20
0
25
50
75
100
Rank
Rank

Fig. S9 Timing of growth arrest in dark-grown *dwf4* mutant hypocotyls.

As *dwf4* homozygous mutants did not produce seed, analysis of growth arrest was performed by comparing wild type with progeny from *dwf4/DWF4* heterozygotes. About 25% of the heterozygote progeny were expected to be *dwf4* homozygotes. (**A** to **E**) Lengths of etiolated wild type (Col-0) hypocotyls at (A) 3 DAS (days after stratification), (B) 4 DAS, (C) 5 DAS, (D) 6 DAS and (E) 7 DAS. (**F** to **J**) Lengths of etiolated hypocotyls from progeny of *dwf4/DWF4* heterozygote at (F) 3 DAS, (G) 4 DAS, (H) 5 DAS, (I) 6 DAS and (J) 7 DAS. Measurements were ranked in order of ascending length. Hypocotyl lengths were indistinguishable between wild type and *dwf4/DWF4* progeny at 3 DAS (compare A and F). By 4 DAS, a sharp transition from short (<2mm) to long (>2mm) hypocotyls was observed for *dwf4*/*DWF4* progeny at about the 25th percentile (arrowed in G), but not in wild type (B). This result suggests that *dwf4* mutant hypocotyls had attained a maximum length of about 2mm at this stage. During later stages, about 25% of hypocotyls remained at < 2mm, while the rest continued to increase in length, attaining a maximum of 15-20 mm at 7 DAS. Thus, plants homozygous for *dwf4* arrested hypocotyl elongation at 4 DAS, at a length of 2mm or less. Images were taken using a flatbed scanner and measurement in ImageJ. Hypocotyl length was measured from the base (where lateral roots emerge) to just below the apical hook.

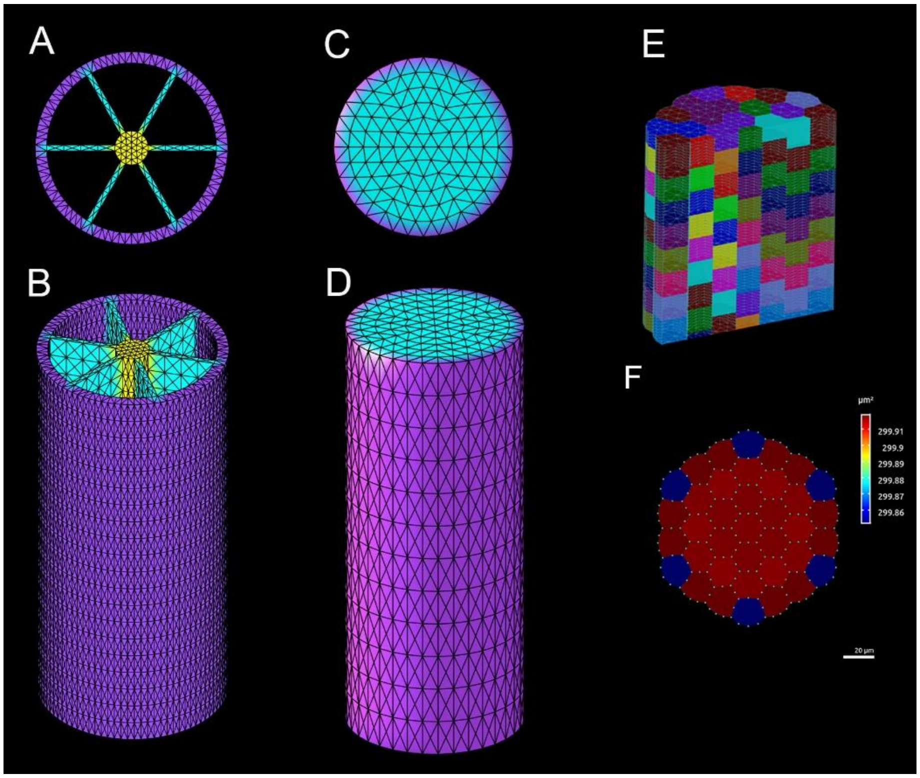

Fig. S10. Meshes of *Utricularia* and *Arabidopsis* models

(**A** and **B**) Initial mesh for *Utricularia* tissue-level models was created with an outer cylinder (epidermis, purple), an axial core (yellow) and six connective blades (cyan). (A) Top-down view. (B) Oblique side view. (**C** and **D**) A solid mesh cylinder consisting of six concentric rings of finite elements used for *Arabidopsis* tissue-level models. The outermost ring was assigned epidermal identity (outer surface purple, inner cyan) and the other rings were treated as inner tissues (cyan). (C) Top-down view. (D) Oblique side view. (**E** and **F**) Template created in CellMaker for cell-level *Arabidopsis* models. (E) Oblique sectional view with cells colored differently. (F) Cross-section showing smoothed hexagonal shape and color-coded according to cell area, from 299.85 to 299.92 µm^2.

References

32. T. Asami et al., Characterization of brassinazole, a triazole-type brassinosteroid biosynthesis inhibitor. Plant physiology 123, 93-100 (2000).
33. E. Truernit et al., High-resolution whole-mount imaging of three-dimensional tissue organization and gene expression enables the study of Phloem development and structure in Arabidopsis. Plant Cell 20, 1494-1503 (2008).
34. S. Strauss et al., Using positional information to provide context for biological image analysis with MorphoGraphX 2.0. Elife 11, e72601 (2022).
35. R. Wightman, S. Wallis, P. Aston, Hydathode pit development in the alpine plant Saxifraga cochlearis. Flora 233, 99-108 (2017).
36. H. Li, N. A. Trzaskalski, R. J. N. Emery, Analysis of Brassinosteroids in Soybean Seeds and Leaves by Liquid Chromatography-Tandem Mass Spectrometry. The Open Plant Science Journal 10, 100-109 (2017).
37. F. Huo et al., A new derivatization approach for the rapid and sensitive analysis of brassinosteroids by using ultra high performance liquid chromatography-electrospray ionization triple quadrupole mass spectrometry. Talanta 99, 420-425 (2012).
38. P. Xin, J. Yan, J. Fan, J. Chu, C. Yan, An improved simplified high-sensitivity quantification method for determining brassinosteroids in different tissues of rice and Arabidopsis. Plant Physiol 162, 2056-2066 (2013).
39. P. Xin et al., A Tailored High-Efficiency Sample Pretreatment Method for Simultaneous Quantification of 10 Classes of Known Endogenous Phytohormones. Plant Communications 1, 100047 (2020).
40. J. P. Blumenstiel et al., Identification of EMS-Induced Mutations in Drosophila melanogaster by Whole-Genome Sequencing. Genetics 182, 25-32 (2009).
41. T. Lan et al., Long-read sequencing uncovers the adaptive topography of a carnivorous plant genome. Proceedings of the National Academy of Sciences 114, E4435-E4441 (2017).
42. D. J. Cosgrove, Diffuse Growth of Plant Cell Walls. Plant Physiol 176, 16-27 (2018).
43. J. A. Lockhart, An analysis of irreversible plant cell elongation. J Theor Biol 8, 264-275 (1965).
44. M. Majda, N. Trozzi, G. Mosca, R. S. Smith, How Cell Geometry and Cellular Patterning Influence Tissue Stiffness. International Journal of Molecular Sciences 23, 5651 (2022).
45. H. Hofhuis et al., Morphomechanical Innovation Drives Explosive Seed Dispersal. Cell 166, 222-233 (2016).
46. G. W. Bassel et al., Mechanical constraints imposed by 3D cellular geometry and arrangement modulate growth patterns in the Arabidopsis embryo. Proceedings of the National Academy of Sciences 111, 8685-8690 (2014).
47. E. Hernandez-Lagana et al., Organ geometry channels reproductive cell fate in the Arabidopsis ovule primordium. Elife 10, e66031 (2021).
48. E. Ibarra-Laclette et al., Architecture and evolution of a minute plant genome. Nature 498, 94 (2013).
49. A. Bajguz, M. Chmur, D. Gruszka, Comprehensive Overview of the Brassinosteroid Biosynthesis Pathways: Substrates, Products, Inhibitors, and Connections. Frontiers in Plant Science 11, (2020).

Table S1. Potential candidates for *ENHANCER OF DWARF*

Coordinates in Chromium genome	Coordinates in PacBio genome	In a coding sequence (CDS)	BLAST results
28566:47991	unitig_46:2492174	Yes	Unidentified mRNA
28615:2102460	unitig_0:3069816	Yes	CWZF3 (Cysteine-tryptophan domain-containing zinc finger protein 3)
78:10266	unitig_8:2737781	Yes	Purine permase 3-like (cytokinin transport)
28603:684091	unitig_5:2804	Yes	Dynamin-related protein 1E (DRP1E) - microtubules

Candidate SNPs were found to be fixed for the mutant allele in extreme mutants, not homozygous for the mutant allele in intermediate mutants or the progenitor, segregated across wild types and had an EMS signature. Gene annotation information was taken from (*49*).

Table S2. Simulation parameters for cellular models

	Outer walls			Inner walls		
	Thickness (nm)	**Extensibility**	**Threshold**	**Thickness (nm)**	**Extensibility**	**Threshold**
Wild type	2000	30	0.01	200	1	0.02
Dwarf	2000	1	0.02	200	1	0.02
Uniform Walls	200	1	0.02	200	1	0.02

Wild type in Fig. 5, S to V. Dwarf in Fig. 5, O to R. Uniform walls in Fig. 5, K to N. All simulations used a longitudinal Young’s modulus of 150MPa, a transverse Young’s modulus of 1050 MPa, a Poisson’s ratio equivalents of 0.3 and a turgor pressure of 0.5MPa.